Pure

University of Dundee

DOCTOR OF SCIENCE

Modification and processing of glass and glass with embedded silver nanoparticles

Fleming, Lauren A. H.

Award date:
2016

Awarding institution:
University of Dundee

Link to publication

Modification and processing of glass and glass with embedded silver nanoparticles

Lauren A. H. Fleming, BSc (Hons)

Supervisor: Professor Amin Abdolvand

A thesis submitted to the School of Science and Engineering, University of Dundee for the degree of Doctor of Philosophy (PhD)

2016

Contents

List of Figures

List of Tables

List of Abbreviations

AFM	Atomic Force Microscopy
dc	Direct Current
DOE	Diffractive Optical Element
EFAD	Electric Field Assisted Dissolution
NBO	Non-Bridging Oxygen
NIR	Near Infrared
NP	Nanoparticle
SEM	Scanning Electron Microscope
SERS	Surface-Enhanced Raman Spectroscopy
SP	Surface Plasmon
SPR	Surface Plasmon Resonance
UV	Ultraviolet
VIS	Visible
wt%	Percentage by Weight

Declaration

I, the undersigned, declare that I am the author of this thesis; that all references cited have been consulted by me, that the work, of which the thesis is a record, has been carried out by myself, and it has not been previously accepted for a higher degree.

Lauren Fleming

Certification

I, Professor A. Abdolvand of the School of Science and Engineering, hereby certify that Lauren Fleming has spent the required number of terms at research under my supervision and that she has fulfilled the conditions of the Ordinance of the University of Dundee so that she is qualified to submit the following thesis for the degree of Doctor of Philosophy.

Amin Abdolvand

List of Publications

The following publications by the author are related to this thesis:

1. L. A. H. Fleming, D. M. Goldie and A. Abdolvand, "Imprinting of glass," Opt. Mater. Express **5**(8), 1674-1681 (2015).

2. L. A. H. Fleming, G. Tang, S. A. Zolotovskaya, and A. Abdolvand, "Controlled modification of optical and structural properties of glass with embedded silver nanoparticles by nanosecond pulsed laser irradiation," Opt. Mater. Express **4**(5), 969-975 (2014).

3. L. A. H. Fleming, S. Wackerow, A. C. Hourd, and A. Abdolvand, "Diffractive optical element embedded in silver-doped nanocomposite glass," Opt. Express **20**(20), 22579-22584 (2012).

Related conference presentations of the author:

4. L. A. H. Fleming and A. Abdolvand, "Nanosecond pulsed laser processing of glass embedded with metal nanoparticles: Fast modification of nanocomposites," EPSRC Manufacturing the Future (2014).

5. L. A. H. Fleming and A. Abdolvand, "Nanosecond pulsed laser irradiation of silver-doped nanocomposite glass," CLEO Europe (2013).

6. L. A. H. Fleming and A. Abdolvand, "2-D structuring of silver-doped nanocomposite glass," Photon, (2012).

Acknowledgements

The research carried out during this PhD would have not been possible without the help and support of so many people. First and foremost I would like to give my deepest gratitude to Professor Amin Abdolvand; my supervisor and head of our group, MAPS, for giving me the opportunity to carry out this research. Thank you for the opportunity to work with you and for your time, advice, motivation and encouragement. Thanks also to the Engineering and Physical Sciences Research Council (EPSRC) for the funding of this project.

I would like to express my thanks to all of the MAPS group; in particular to Professor Allan Gillespie for his guidance and support throughout, to Dr Allan Hourd for always lending an ear or a hand, Dr Youngchang Fan for his technical help, and to Dr David Goldie for his direction on the measurement of conductivity and continuing support. I'd like to thank the rest of my MAPS colleagues; Mateusz Tyrk, Dr Fu Yu, and Dalong Zang for being so kind and helpful, Dr Svetlana Zolotkovskaya for her help with laser processing and for her assistance illustrating the aesthetic properties of this process, Dr Stefan Wackerow for his tuition from the very beginning of this work, Dr Guang Tang for his help with laser processing and the temperature modelling it required, and my friend Stephen Grant who was a pleasure to sit beside every day and never seemed to tire of my endless rambling.

I wish to express my thanks to the technicians at the University of Dundee; especially to Gary Callon, Callum Moore and Stuart Anthony for

their assistance with a special mention for Grant Kidd. I would like to extend my thanks to all of the University of Dundee Physics Department which is full of the most friendly and helpful staff.

On a more personal note; thank you to my friends, in particular David and Kyle, thanks for always being there with an ear, a laugh or a drink. Thank you to the members of the Dundee University Surf club; I may still be a bit of a noob but you brought me some of my best times over the past few years.

Finally, I would like to thank my family. To my Dad, John; you may not say much but with what you have said you have pushed me to be a better person and to achieve more; even when I didn't think I could. To my Mum, Angela; I know I can always count on you for endless support no matter what I do, thank you for always being there. To my Granny, Ann; you believe in me even when I don't believe in myself. You might just be the best person ever, thank you for everything, keep being brilliant. To my brother, Shane, and my sisters Caron, Nathalie and Rachael; you all helped mould me into the person I am today and I know I can count on you lot to put a smile on my face. To all my family; you are fantastic and there is no way I would be where I am without you.

Thank you, all of you.

Abstract

Glass is an inexpensive and readily available material making it an indispensable element in the many fields of science and technology. This thesis describes three methods of manipulating the optical and structural properties of glass and nanocomposite glass for varying applications. These are: thermal poling of glass, electric field assisted dissolution of glass embedded with silver nanoparticles and the irradiation of glass embedded with silver nanoparticles. Each method will be adapted to present novel and widely applicable approaches to the modification of glass.

Thermal poling of glass will be used to create diffractive optical elements (DOEs) in soda-lime float glass. Thermal poling of glass results in a change to the glass structure, by using an electrode with a periodic pattern the glass was selectively restructured creating an effective DOE. The parameters of the process, namely applied voltage and temperature, were investigated for their part in the efficiency of the resultant DOE.

A second method for the fabrication of DOEs will use electric field assisted dissolution (EFAD) of glass embedded with spherical silver nanoparticles. This process leads to the dissolution of silver nanoparticle into the surrounding glass. By selecting a mesh electrode with a periodic pattern an effective DOE was fabricated by selectively dissolving the silver nanoparticles in contact with the electrode. As with thermal poling, the voltage and temperature of the process will be investigated in order to produce more efficient DOEs.

Glass with embedded spherical silver nanoparticles was irradiated using a nanosecond (36 ns) pulsed laser at 532 nm. Laser irradiation led to the formation of a thin surface film containing uniformly distributed nanoparticles - with an increase in the overall average nanoparticle size. The influence of the applied number of laser pulses on the optical and structural properties of such a recipient nanocomposite was investigated.

Statement of Author's Contribution

Below is a list of the contributors to the work presented with the highest contributor first and decreasing:

Name	Role	Contribution
Lauren Fleming	Principle author	Setup and conducted all experiments, performed analysis on all samples, interpreted data, wrote manuscript.
Prof Amin Abdolvand	Principle supervisor	Provided supervision and guidance.
Dr David Goldie	Contributor	Provided test equipment and guidance for conductivity measurements and calculations.
Dr Stefan Wackerow	Contributor	Provided guidance for experimental portions.
Dr Guang Tang	Contributor	Provided guidance for laser processing and temperature modelling.
Dr Svetlana Zolotovskaya	Contributor	Provided guidance for experimental portions.
Dr Andrew Hourd	Contributor	Supervisor when using hydrofluoric acid and provided guidance for experimental portions.

Chapter 1: Introduction

Glass as a material is used in a variety of products. In many cases, the properties of a glass product may be optimized; by changing the chemical composition of the glass by introducing other materials, and effects can also be achieved by changing the physical and optical structure of the glass.

Altering the physical structure of the glass is widely desirable and has been achieved in a range of methods with varying degrees of accuracy. Thermal poling [1-6] is perhaps one of the most well-known and reliable glass modification processes and involves high temperatures along with the application of a dc (direct current) electric field to alter the structure of the glass.

The distinctive properties of metallic nanoparticles embedded within glass have sparked significant interest due to the unique linear and nonlinear optical properties that this composite material possesses. These properties are dominated by the strong surface plasmon resonances (SPRs) of the metal nanoparticles and it is possible to design the position of these SPRs within a wide spectral range by manipulation of size [7], shape [8], and spatial distribution [9] of the embedded particles, making modification of these particular materials of great interest.

This thesis will present novel approaches to both thermal poling and the modification of glass embedded with silver nanoparticles.

1.1.   Objectives of this work programme

Firstly thermal poling will be used for the fabrication of effective diffractive elements from *common soda-lime float glass*. Diffractive elements are typically fragile and costly to fabricate to a large scale. However it will be shown that by using an applied dc electric field across the glass at reasonably elevated temperatures it is possible to create effective diffraction gratings that are both cost efficient and robust in a process that is simple and reproducible. The effect of using high temperature and applied electric field results in a restructuring of the glass matrix which alters the glass refractive index. By using a patterned electrode, the electric field is selectively applied to the glass and thus creates periodic variations in the refractive index, *via redistribution of the alkali ions*, throughout the final product. This periodic change in the refractive index of the glass is responsible for the diffraction patterns shown. The diffraction pattern is therefore dictated by the easily modified pattern of the electrode, allowing for this technique to be used for the cost effective production of complex, large-scale diffractive optical elements using a simplistic and reliable process.

The second method will describe the use of thermal poling on *glass with embedded silver nanoparticles*; more commonly known as electric field assisted dissolution (EFAD) [10, 11]. By employing the EFAD process, with a patterned electrode, diffractive optical elements were fabricated in this stable and unique material. In this instance rather than restructuring the glass itself as with thermal poling, EFAD causes the selective dissolution of the silver nanoparticles into the surrounding glass providing an embedded grid of clear glass where there had been contact between the glass composite and the patterned electrode. This periodic pattern allows the material to function as a diffraction grating. Optimisation of the

process is presented demonstrating that higher voltage, or temperature, during the fabrication leads to more complete dissolution of the silver nanoparticles. It will be shown that this technique is suitable for the low-cost fabrication of efficient and robust diffractive optical elements.

For the final technique described, *glass with embedded silver nanoparticles* was modified by use of nanosecond pulsed Nd:YVO$_4$ laser irradiation. This resulted in the formation of a reflective surface film and an increase in the nanoparticle size following irradiation. By varying the number of pulses applied per spot it was discovered that with increasing number of pulses there is an increase in the average nanoparticle radius. The temperature rise during the irradiation process was calculated to be well above the glass softening temperature, implying that during irradiation the glass, and the silver embedded within it, are in the molten phase. This localized melting and reforming of the glass is tightly controlled and along with the simplicity and flexibility of the process leads to nanosecond pulsed laser irradiation being a suitable technique for the creation of complex, reproducible patterns of larger nanoparticles with smaller separation distances in glass embedded with silver nanoparticles. This allows for the tuning of the optical and structural properties of metal-glass nanocomposites, making this process suitable for the fabrication of complex optical elements, aesthetic products and sensing applications.

1.2. Chapter outline

Before describing the work involved, Chapter 2 serves as an introduction to the topic followed by an overview of glass embedded with metallic nanoparticles, and specifically silver nanoparticles. Chapter 3 is a description of the effective medium theory used to describe the electromagnetic properties of composite materials, in this case the Maxwell-Garnett theory. Subsequent chapters are devoted to each of the

methods described above: Chapter 4 will describe the thermal poling process involved in creating diffractive optical elements in soda-lime float glass; Chapter 5 will then use a similar process employing glass embedded with silver nanoparticles to fabricate more efficient diffractive optical elements, and Chapter 6 provides an analysis of laser processing of glass embedded with silver nanoparticles. Chapter 7 concludes the work and suggests possibilities for future research in this area.

Chapter 2: Introduction to properties of glass embedded with metallic nanoparticles

In this chapter the characteristics of metal nanoparticles are presented, focusing on their optical properties and how they react with light. This is followed by a brief history of their uses when embedded in dielectric media, namely glass, and the unique optical phenomena that result. This section will also include an introduction to glass embedded with silver nanoparticles which was used throughout this work.

2.1. Metallic nanoparticles

2.1.1. Introduction

Nanoparticles are defined as being particles between 1 and 100 nanometres in size, a particle being a fragment of matter which acts as a whole unit with respect to its properties. Nanoparticles are of great interest as their nanoscale size allows them to exhibit pronounced phenomena including optical, structural and electronic effects not seen in the bulk form of the material. The unique properties of nanoparticles make them an area of intense interest due to a wide variety of potential applications not only across the field of physics [12, 13], but also in life sciences [14-17] and chemistry [18], contributing to an ever growing area of research.

Metal nanoparticles have attracted much attention over the last decade owing to their unique properties as compared to their bulk metal equivalents. A vital aspect of their application potential is the ability to control the properties of nanoparticles

with particular respect to size, shape and spatial distribution where the nanoparticles are embedded within a host medium. Recent advances in controlling the shape and size of nanoparticles have opened the possibility to optimise the particle geometry for applications [7, 19, 20].

Bearing in mind the advantages and many outstanding features of metal nanoparticles, it is hardly surprising that the number of publications which involve these materials has increased almost exponentially over the last few years (Fig. 1). Research efforts are expected to continue to increase as the benefits become increasingly apparent for applications across many fields.

(a)   (b)
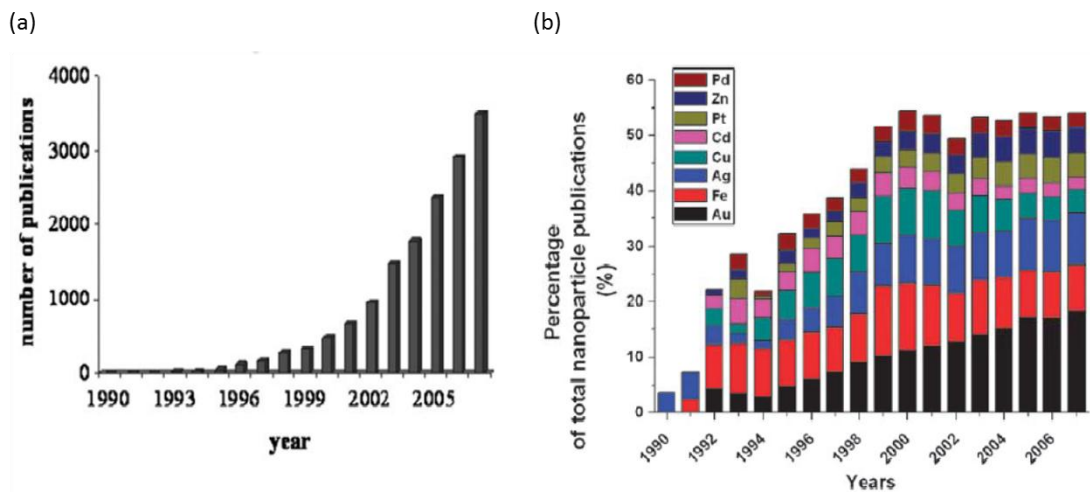
Fig. 1. (a) The growth of number of publications concerning metallic nanoparticles [21]. (b) Interest in specific elements in the preparation of nanoparticles [22].

A significant amount of research has been devoted to controlling the dimensions and spatial distributions of metallic nanoparticles embedded within glass and other dielectric media [23-26]. This is due specifically to the unique optical phenomena they present. These are directly related to the specific particle morphology (size and shape), metal dispersion, concentration and the electronic

properties of the metal within their host environment. Control of the size, shape and dispersion of embedded nanoparticles is the key to the selective and enhanced optical properties that can be achieved.

2.1.2. Properties

One of the characteristic features of metal materials is their ability to act as conducting media. As with all conducting materials this is achieved by the presence of free electric charges, which for metals are normally electrons, the motion of which constitutes a current.

The current per unit area, J, resulting from the application of an electric field, $\vec{E}$, is related to the conductivity of the medium, σ, by Ohm's Law, $J = \sigma\vec{E}$. For dielectric materials there are no free electric charges to carry the current so $\sigma = 0$. However, as metals have the presence of electric charge carriers in the form of conduction electrons σ is nonzero and constant.

2.1.3. Interaction with light

For the most part any interaction between light and metals takes place between the optical electric field and electrons in the conduction band (i.e. electrons have sufficient energy to move freely through the material). However, some of the light energy can be transferred to the bulk material when a collision takes place (energy in the form of heat). It is reasonable to characterise the optical properties of metals by use of two optical constants; the refractive index, n, and the extinction coefficient, κ. These result in the complex refractive index, $\tilde{n}$, where;

$$\tilde{n} = n + i\kappa, \qquad\qquad 1$$

n is defined as the ratio of the phase velocity of light in a vacuum to its phase velocity in a specified medium. κ indicates the amount of attenuation when the electromagnetic wave propagates through the material. Both these constants may vary with wavelength and temperature [27] and therefore the expression for an electromagnetic wave propagating in an absorbing medium contains both of these parameters. By relating the complex wave number $\tilde{k}$ to $\tilde{n}$ through $\tilde{k} = 2\pi\tilde{n}/\lambda_0$, with λ_0 being the vacuum wavelength; this can be inserted into the plane wave expression as;

$$E(x,t) = \mathrm{Re}\left[E_0 e^{i(\tilde{k}x - \omega t)} \right] = \mathrm{Re}\left[E_0 e^{i\left(\frac{2\pi(n+i\kappa)x}{\lambda_0} - \omega t \right)} \right] = e^{-2\pi\kappa x/\lambda_0} \, \mathrm{Re}\left[E_0 e^{i(kx - \omega t)} \right],$$

2

where E_0 is the amplitude of the wave measured at the point $x = 0$ in the medium, $E(x,t)$ is the instantaneous value of the electric vector measured at a distance x from the first point and at some time t, ω is the angular frequency of the source, k is the wave number, and λ_0 is the wavelength in vacuum.

The absorption coefficient, α, is related to the extinction coefficient by:

$$\alpha = 4\kappa/\lambda_0 .$$

3

The absorption coefficient can be used in order to obtain the light intensity, I, as it varies with depth, z, by employing Beer's equation;

$$I(z) = I_0 e^{-\alpha z} ,$$

4

where I_0 is the intensity of the incident light. Note that this equation assumes that both the incident intensity and the intensity measured at depth z are measured *within* the absorbing medium. Beer's equation demonstrates that after the wave has propagated a distance of $z = 1/\alpha$ the intensity of the incident wave (the flux density) will drop by a fact of e^{-1}, this is known as the penetration depth (or skin depth). The

penetration depth for transparent dielectrics is larger than the thickness of the material; however the penetration depth for metals is very small. For example, copper has a penetration depth of only 6 nm for light at 10 μm which drops to only 0.6 nm for ultraviolet light at 100 nm [12].

The relationship between the flux density (light intensity) and the optical constants can be described by using the complex dielectric constant of the material. The dielectric constant is the ratio of the permittivity of a substance to the permittivity of free space. The complex dielectric constant, ε_i, is given by;

$$\varepsilon_i = \varepsilon' + i\varepsilon'', \qquad 5$$

where ε' and ε'' denote the real and imaginary parts of the dielectric constant respectively. The real and imaginary dielectric constants are related to the previously mentioned optical constants, the refractive index and extinction coefficient, by;

$$\varepsilon' = n^2 - \kappa^2, \qquad 6$$

$$\varepsilon'' = 2n\kappa. \qquad 7$$

2.2.   Glass embedded with metallic nanoparticles

2.2.1.   Introduction

Glasses with embedded metallic nanoparticles are of particular interest due to the unique optical phenomena they present. These optical properties have been employed for centuries in order to provide a desired aesthetic effect, although not fully understood until much later. An example of this can be seen in the Lycurgus cup (Fig. 2 (a)), a 4th century Roman glass cup made of dichroic glass which shows a different colour depending on whether or not light is passing through it; appearing green when illuminated from the front (Fig. 2 (a(i))) and red when lit from behind

(Fig. 2 (a(ii))). This effect is due to nanoparticles of gold and silver which are present in the glass. When light is passing through the material the gold and silver nanoparticles absorb green and blue light making the cup appear red. It is likely that the glass makers knew little about this effect and that the addition of gold and silver nanoparticles may not have even been controlled and was probably discovered by accidental "contamination" with ground gold and silver particles produced by other work being carried out in the vicinity.
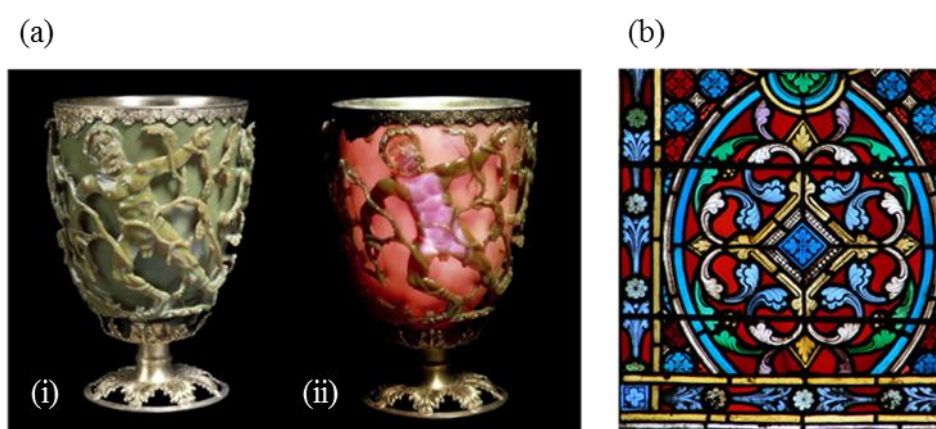
Fig. 2. (a) The Lycurgus cup (4th century) appears a different colour when illuminated (i) from the front and (ii) from behind due to the presence of gold and silver nanoparticles which are thought to have been added accidentally during the glass manufacturing process. (b) By the 19th century bold colours were being proposedly achieved in stained glass panels, like those on display at Meaux Cathedral in France, by adding metallic oxide powders which were known to produce vivid colours.

Some of the earliest known examples of *purposefully* adding metallic nanoparticles can be seen in stained glass windows, Fig. 2 (b). Growing in popularity during the medieval times, glass was coloured using metallic oxide powders with certain types of metals known for producing particular colours; copper producing

green, cobalt making blue, and gold providing a red or violet colour. Silver stain was introduced later and provided a much sought after strong yellow colour.

More recently glasses with embedded silver nanoparticles have been of interest as the optical effects become better understood, enabling these materials to be used in many applications.

2.2.2. Optical properties of glasses embedded with metallic nanoparticles

The unique linear and nonlinear optical properties of glasses embedded with metallic nanoparticles are dominated by the strong surface plasmon resonances (SPRs) of the metal nanoparticles.

Exposure of a metal nanoparticle to an electric field results in a shift of the free conduction electrons within the nanoparticle. The surface charges of opposite sign on the opposite surface elements of the particles (see Fig. 3) produce a restoring local field within the nanoparticle. The shifted electrons of the metal particle, together with the restoring field consequently represent an oscillation. The combined oscillation of many electrons constitutes surface plasmon resonance [12, 34].
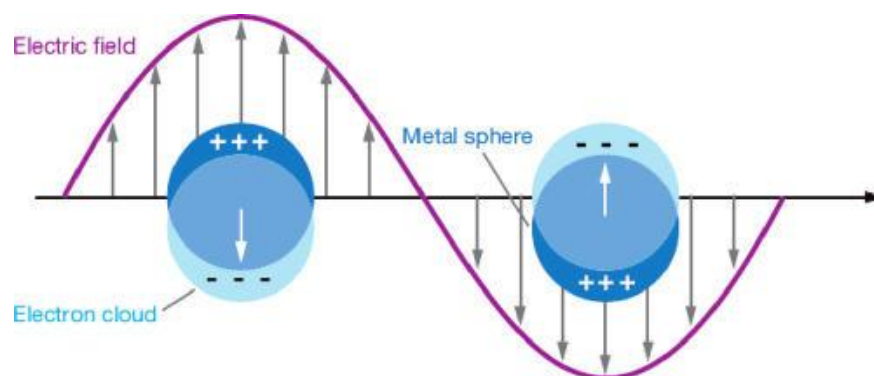
Fig. 3. An illustration of an electromagnetic wave inducing the surface plasmon oscillation of metallic nanoparticles.

The spectral position and shape of SPRs can be designed within a wide spectral range throughout the visible and near-infrared spectrum by choice of metal [12], Fig. 4. (a), and host matrix [28], Fig. 4 (b).
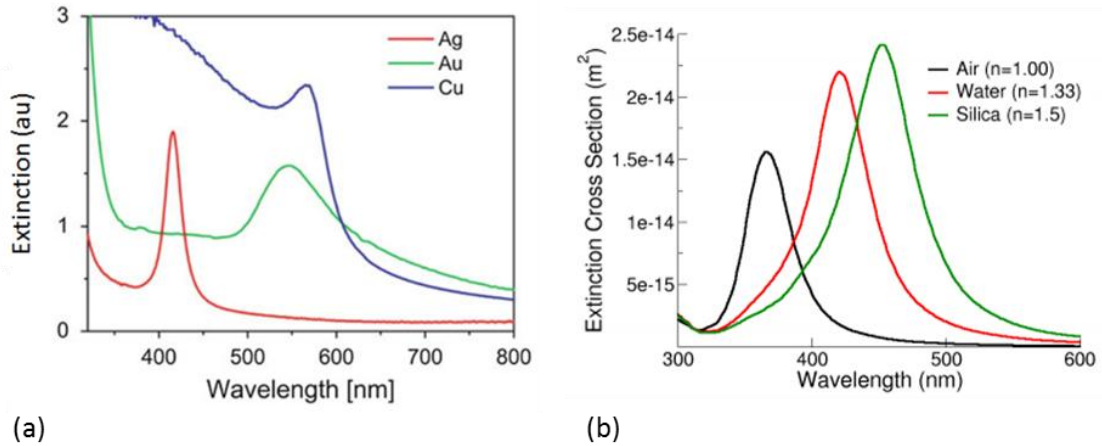
Fig. 4. (a) Extinction spectra of glass containing spherical silver, gold and copper nanoparticles [29]. (b) Extinction spectra of silver nanoparticles in different host media.

The properties of the SPR are also heavily dependent on the size [7], shape [30], spatial distribution [31] and concentration (i.e. volume filling factor) [32] of the metal inclusions, these variables are all easily tailored making these composites a desirable material for many applications in the field of photonics.

The Mie solution to Maxwell's equations for the scattering and absorption of light by spheres provides an exact analytical theoretical description of surface plasmons of spherical metals nanoparticles [12, 33, 34]. For particles which are small compared to the local variations of the involved electromagnetic fields, the quasistatic approximation [12] is valid; this approximation assumes the exciting field is homogeneous and uniform over the particle's volume.

Under these assumptions, the results of electrostatics can be applied by using the corresponding frequency dependent dielectric function. In this case, the

polarizability, *a,* and induced dipole moment, *p,* of an embedded metallic sphere in a

dielectric medium are:

$$a = 4\pi R^3 \frac{\varepsilon_i(\omega) - \varepsilon_h}{\varepsilon_i(\omega) + 2\varepsilon_h} ,$$

8

$$\vec{p}(\omega) = a\varepsilon_0 \vec{E_0}(\omega) = 4\pi\varepsilon_0 R^3 \frac{\varepsilon_i(\omega) - \varepsilon_h}{\varepsilon_i(\omega) + 2\varepsilon_h} \vec{E_0}(\omega) ,$$

9

where R is the radius of the nanoparticle, E_0 the electric field strength of an incident

electromagnetic wave, ε_0 the electric permittivity of vacuum, and $\varepsilon_i(\omega)$ and ε_h are,

respectively, the relative complex electric permittivity of metal and host matrix.

The absorption cross section, $\varsigma(\omega)$, of a spherical metal inclusion placed in a

transparent dielectric matrix, where the imaginary part of the relative complex

electric permittivity approaches zero ($\text{Im}[\varepsilon_h] \to 0$) is then given as:

$$\varsigma(\omega) = 12\pi R^3 \frac{\omega}{c} \varepsilon_h^{3/2} \frac{\varepsilon_i^{''}(\omega)}{\left[\varepsilon_i^{'}(\omega) + 2\varepsilon_h\right]^2 + \varepsilon_i^{''}(\omega)^2} ,$$

10

where c is the speed of light $\varepsilon_i{'}(\omega)$ and $\varepsilon_i{''}(\omega)$ are real and imaginary part of the

electric permittivity of the metal and combined can be described by the Drude-

Sommerfeld formula:

$$\varepsilon_i(\omega) = \varepsilon_b + 1 - \frac{\omega_p^2}{\omega^2 + i\gamma\omega} .$$

11

Here, γ is a damping constant of the electron oscillations and ε_b is the complex

electric permittivity associated with interband transitions of the core electrons in

atom. The free electron plasma frequency, ω_p, is given by:

$$\omega_p = \sqrt{\frac{Ne^2}{m^*\varepsilon_0}} ,$$

12

where N is the density of the free electrons, e is the electron charge and m^{*} is the effective mass of the electron (the mass that the electron appears to have when responding to forces in a given medium).

From Eqs. 8-10, Mie resonance occurs at the surface plasmon (SP) frequency, ω_{SP}, under the following conditions [29]:

$$\left[\varepsilon_i^{'}(\omega) + 2\varepsilon_h \right]^2 + \varepsilon_i^{''}(\omega)^2 \rightarrow Minimum . \qquad 13$$

If the imaginary part of the electric permittivity of the metal is small in comparison with the real component, or has a small frequency dependency, then Eq. 13 can then be written as:

$$\varepsilon_i^{'}(\omega_{SP}) = -2\varepsilon_h . \qquad 14$$

If Eq. 14 holds true; the dipole moment and local electric field in the vicinity of the nanoparticle grow significantly and can overcome the field of the incident wave. This phenomenon is responsible for the SP enhanced nonlinearities of the metal composite material.

Each of the noble metals has a specific surface plasmon absorption band. For instance, silver nanoparticles embedded in a glass matrix exhibit an SP band at about 417 nm, as can be seen from the extinction spectra presented in Fig. 5. However, for Au and Cu nanoparticles embedded in glass the SP band is shifted towards the red spectral range and peaks at around 528 nm and 570 nm, respectively. The broad absorption bands below 500 nm for glasses containing either Au or Cu are associated with interband transitions, namely from d- to s-shell, due to the absorption of light at these energies. However, for silver the interband resonance is peaked at 310 nm (4 eV) far away from the SP resonance [35].
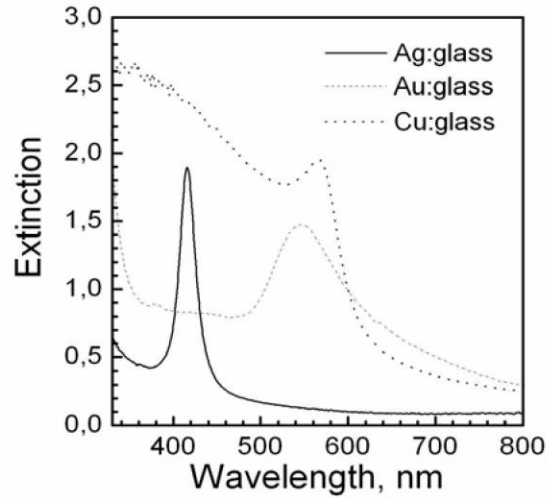
Fig. 5. The extinction spectra of glass which contains spherical silver, gold and copper nanoparticles.

Using Eq. 14 and by substituting the real part of the metal electric permittivity from Eq. 11, the position of the SP resonance can be expressed as follows:

$$\omega_{SP}^2 = \frac{\omega_p^2}{\text{Re}\left[\varepsilon_b\right]+1+2\varepsilon_h} - \gamma^2.$$

15

From Eq. 15, it can be gathered that the core electrons have a significant influence on the surface plasmon resonance and therefore define the position of the SP band in the extinction spectra (Fig. 5) for different noble metals. Eq. 15 also describes a dependence of the SP resonance on the dielectric properties of the host medium which the metal nanoparticles are incorporated within. An increase of dielectric constant (refractive index) evokes the shift of absorption peak towards long wavelengths [12, 36, 37] (as seen in Fig. 6).
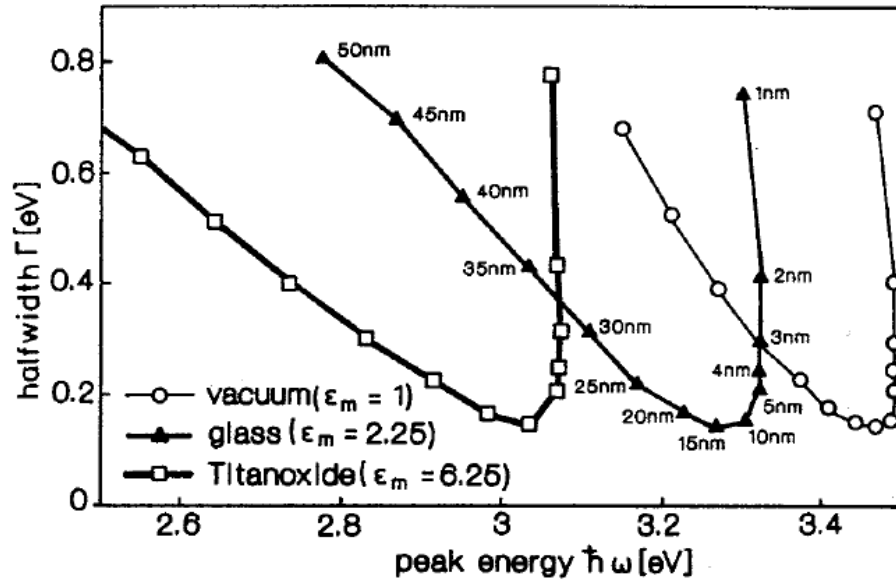
Fig. 6. Halfwidth of the surface plasmon resonance of silver nanoparticles versus the respective peak energy shown for varying embedding media (vacuum, glass, and TiO₂) and particle size (shown as markers on the curves, separation between particles is kept constant). This figure is adapted from [12].

The curves in Fig. 6 [12] represent the calculated spectral positions of surface plasmon resonances of silver nanoparticles contained within three different media: vacuum ($\varepsilon_h = 1$), glass ($\varepsilon_h = 2.25$), and TiO$_2$ ($\varepsilon_h = 6.25$). These results indicate that the SPR peak is more red-shifted for nanocomposites where the embedding media has a higher dielectric constant.

Fig. 6 also shows that the position of the SP resonance depends on the size of the embedded metallic nanoparticles. Although the position remains almost constant for nanoparticles with a radius smaller than 15 nm, the band halfwidth for these clusters differs by a factor of 4. This is often described as an intrinsic size effect [12, 38, 39]. If the particle size is less than that of the mean free path of the electrons in the metal (≈10-15 nm) [40], the electron scattering at the particle surface causes an increase dielectric function, mostly in the imaginary component. For smaller

particles (> 1 nm) the spill-out of electrons from the particle surface should be taken into account, which results in an inhomogeneous dielectric function. As a result, very broad plasmon bands are observed for small nanoparticles (Fig. 6).

On the other hand, for spherical nanoparticles with an increase in radius of greater than 15 nm there is a shift in the SP resonance towards longer wavelengths with simultaneous increase in the band halfwidth (Fig. 6 and Fig. 7). This larger nanoparticle effect is referred as the extrinsic size effect [12, 38, 41, 42]. Here, higher-order (such as quadrupolar) oscillations of conduction electrons become important. Additionally to the red shift and broadening of SP band, Fig. 7, for silver shows also the second peak in extinction spectra, which is the result of these quadrupole effects.
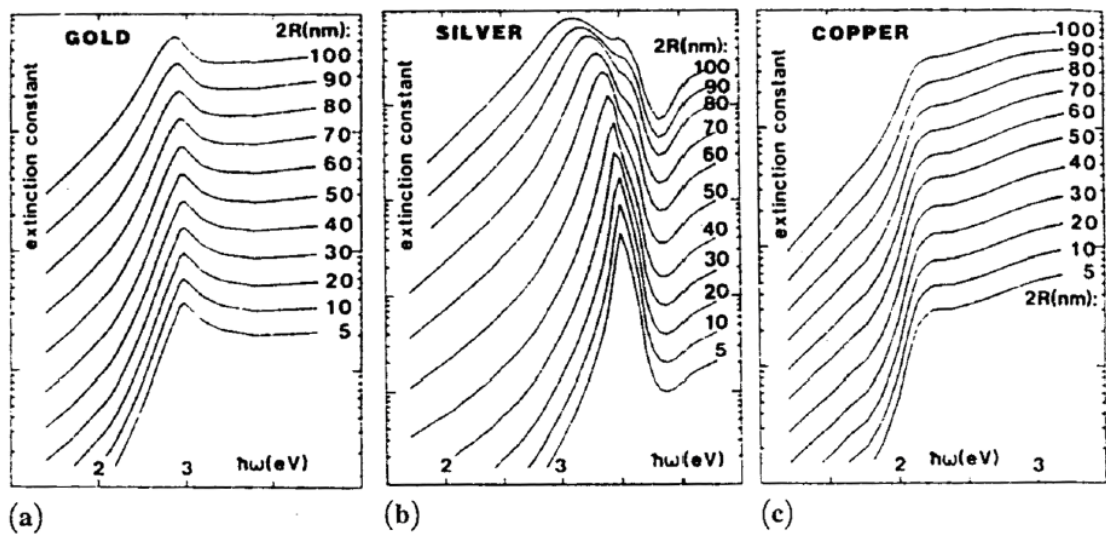
Fig. 7. Calculated Mie extinction spectra of spherical nanoparticles of various metals. Parameter is the size 2R. $\varepsilon_h = 1$. The figure is adapted from [**Error! Reference source not found.**].

Fig. 5, Fig. 6 and Fig. 7 demonstrate the importance of the choice of embedded nanoparticle and nanoparticle size when using glasses embedded with metallic nanoparticles. Silver nanoparticles show a useful pronounced SPR peak due

to a lower peak absorption for interband transitions when compared to copper and gold nanoparticles. It is for this reason that glass embedded with silver nanoparticles will be used for the experimental portions of the presented work. It has also been shown that the nanoparticle size and concentration (or filling factor) plays an important role in the properties of the nanocomposite material and it is therefore desirable to control the nanoparticle properties either during the fabrication process or by post-manufacture processing.

2.2.3.   Production of glass embedded with silver nanoparticles

All of the samples used in the experiments described were prepared from soda-lime float glass (72.5 SiO_2, 14.4 Na_2O, 0.7 K_2O, 6.1 CaO, 4.0 MgO, 1.5 Al_2O_3, 0.1 Fe_2O_3, 0.1 MnO, 0.4 SO_3 in wt%) by Ag^+-Na^+ ion exchange. For the ion exchange process glass substrate is placed in a mixed melt of $AgNO_3$ and KNO_3 at 673 K [36]. The thickness of the glass substrate, time of the ion exchange process, and weight concentration of AgNO3 in the melt determine the concentration and distribution of Ag^+ ions in the glass. Thermal annealing of the ion exchanged glass in H_2 reduction atmosphere (typically at $673 - 723$ K) results in the formation of spherical silver nanoparticles. Samples were characterised using a JASCO V-670 UV/VIS/NIR spectrophotometer, KEYENCE Digital Microscope VHX-1000, and a Hitachi S-4700 field emission scanning electron microscope (SEM).
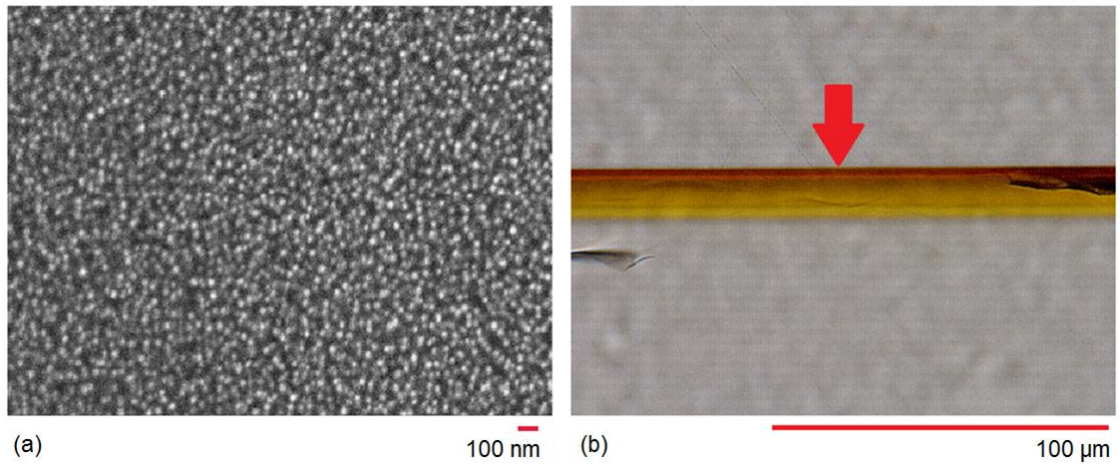
Fig. 8. (a) SEM image of glass with embedded spherical silver nanoparticles. The silver particles are ~30-40 nm mean diameter and are recognisable as white spots. The nanoparticle-containing layer is 20-30 nm beneath the surface of the glass. (b) A thin slice showing the cross-section of the nanoparticle-containing layer. The volume-filling factor of the layer reduces to zero within a few microns and has an exponential decay like profile [8] with the maximum just beneath the surface of the sample which is indicated by a red arrow.

In order to visualize the depth profile of the silver particle-containing layer, one of the samples was cut and a thin slice was prepared. For this the sample was embedded in an epoxy resin (Specifix-20, Struers Limited) to prevent chipping of the glass and to make it physically manageable for grinding and polishing. The resin was allowed to cure at room temperature before the sample was polished on both sides. The resultant slice was ~ 30 µm thick and can be seen in Fig. 8. (b).

As would be expected, size and distribution of Ag nanoparticles (NPs) in the depth of the glass sample depend strongly on temperature and time of Na-Ag ion exchange as well as on the annealing time. For the samples produced here the spherical Ag nanoparticles were 30-40 nm in mean diameter (Fig. 8. (a)) and were distributed in a thin surface layer of approximately 6 µm thickness (the total

thickness of the glass plate was 1 mm). The volume filling factor, *f,* of Ag NPs, defined as the volume of the inclusions per unit volume of the composite material;

$$f = {V_{Ag}} \Big/ {V_{total}}$$

16

was highest just below the glass surface and decreased in an exponential decay like fashion to ~0 within a few microns [8]. This is visible in Fig. 8 (b) as the shade of the nanoparticle containing region is darkest at the surface and grows lighter in the direction of the bulk glass.

The saturated extinction spectrum of this sample of glass embedded with silver nanoparticles is shown in Fig. 9.
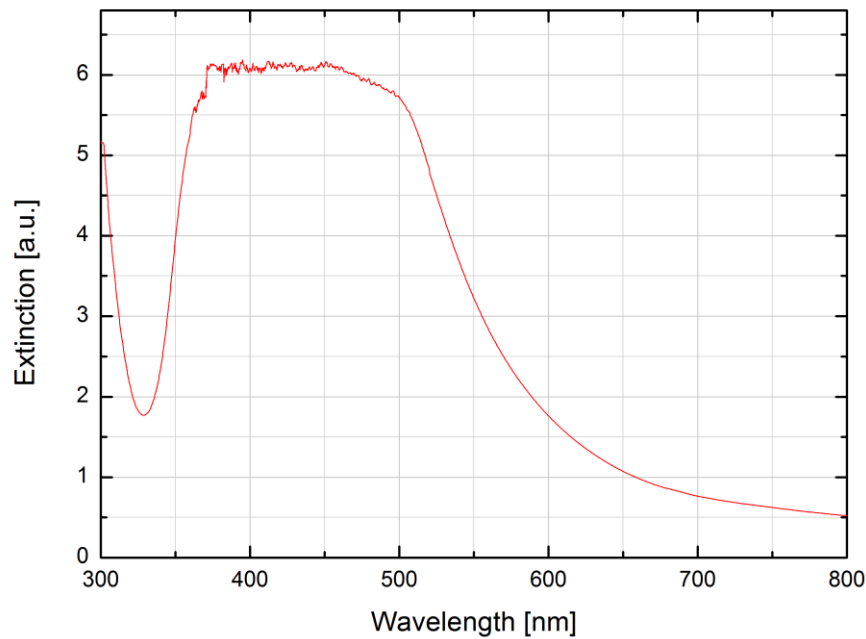
Fig. 9. The saturated measured extinction spectra of glass embedded with silver nanoparticles.

2.3. Maxwell-Garnett theory and optical properties of glass embedded with metallic nanoparticles

There are many different effective medium theories used for modelling electromagnetic properties of composite materials. One of them is Maxwell-Garnett theory [43], renowned for being simple and convenient for modelling, it is widely applied to describe the optical properties of metal particles in dielectric matrices [28, 34, 44]. Although it does not correctly take into account the multipolar interactions between nanoparticles considered in other works [45-47], Maxwell-Garnett theory will be used in this work as it adequately describes the position and shape of the SP resonance and its dependence on the metal filling factor, Eq. 16 [28].

This chapter aims to give a suitable description of Maxwell-Garnett theory and, in particular, show the application of this theory with respect to glass embedded with silver nanoparticles with varying volume filling factor, i.e. nanoparticle concentration.

One of the most important parameters when selecting a glass embedded with silver nanoparticles is the nanoparticle content concentration; any changes in the fraction of metal nanoparticles within the dielectric medium can drastically affect the materials optical properties, Fig. 10. Increasing fraction of metal nanoparticles in a medium leads to the decrease of average particle distances.
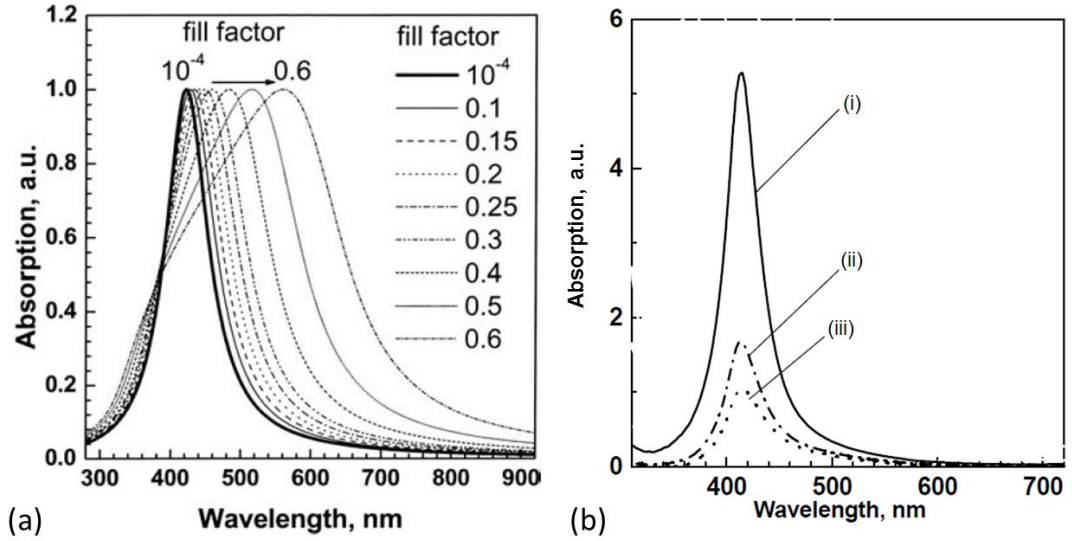
Fig. 10 – The extinction spectra of glass embedded with varying filling factor of silver nanoparticles (a) according to Maxwell-Garnett theory and (b) experimentally measured glass embedded with silver NPs with an estimated filling factor of (i) 0.08, (ii) 0.02, and (iii) 0.006 [8].

According to Maxwell-Garnett theory the effective dielectric constant $\varepsilon_{eff}(\omega)$ of a composite material with spherical metal inclusions having a fill factor f is given by the expression [9];

$$\varepsilon_{eff}(\omega) = \varepsilon_h \frac{\left(\varepsilon_i(\omega) + 2\varepsilon_h\right) + 2f\left(\varepsilon_i(\omega) - \varepsilon_h\right)}{\left(\varepsilon_i(\omega) + 2\varepsilon_h\right) - f\left(\varepsilon_i(\omega) - \varepsilon_h\right)}.$$ 17

here $\varepsilon_i(\omega)$ and ε_h are the complex dielectric constant of the metal and surrounding matrix, respectively and ω denoted the frequency. The complex index of refraction of a composite medium, Eq. 1, can be rewritten as;

$$n(\omega) = n' + in'' = \sqrt{\varepsilon_{eff}(\omega)}.$$ 18

Hence, the absorption coefficient α_{ext} and refractive index n' of the medium with dielectric constant $\varepsilon_{eff}(\omega)$ can be expressed as

$$\alpha_{ext} = \frac{2\omega}{c} \mathrm{Im}\sqrt{\varepsilon_{eff}(\omega)},$$ 19

$$n'(\omega) = \operatorname{Re}\sqrt{\varepsilon_{eff}(\omega)}\,, \qquad\qquad 20$$

where c is the light velocity. Due to variations in the calculated spectra for the absorption and dispersion there is a resultant variation in the reflection properties as a function of filling factor which can be expressed using the complex refractive index:

$$R(\omega) = \left|\frac{n(\omega)-1}{n(\omega)+1}\right|^2. \qquad\qquad 21$$

The reflection spectra (Fig. 11) were calculated as a function of volume filling factor of metal clusters in the glass matrix using the following variables: $\varepsilon_h = 2.3$, $\omega_p = 9.2$ eV, $\gamma = 0.5$ eV [47], $\varepsilon_b = 4.2$ [48].
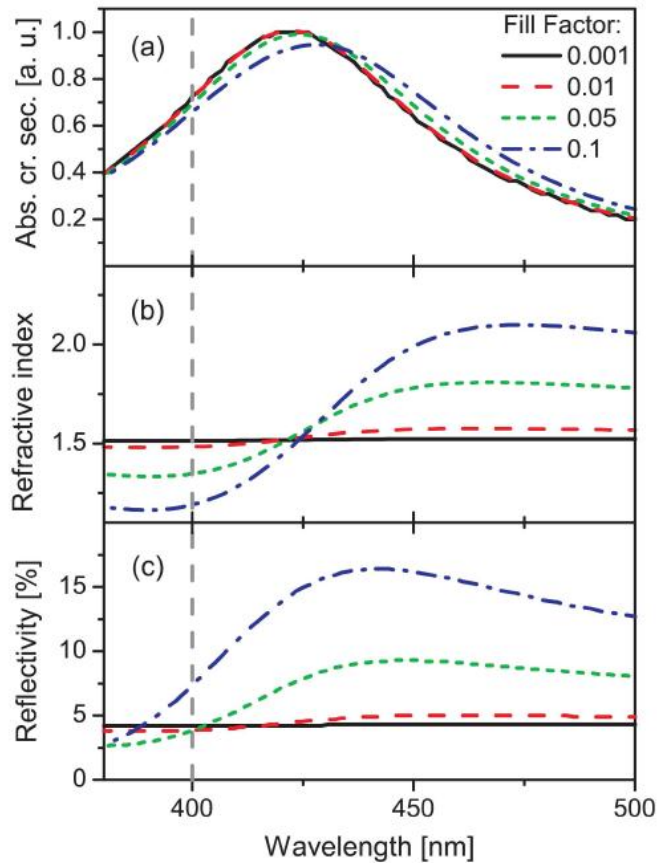
Fig. 11. (a) – Absorption cross-section, (b) – dispersion and (c) reflection spectra of composite glass containing Ag nanoparticles calculated using Maxwell–Garnett theory.

The spectra in Fig. 11 (a) show that dipolar interactions between nanoparticles cause a broadening and red shift of the absorption band with increasing filling factor of silver inclusions in the glass matrix. From Fig. 11 (b) it is noted that at low levels of silver nanoparticle content within the glass ($f = 0.001$) the refractive index is actually identical to that of clear glass ($n' = 1.52$), however higher levels of fill factor results in significant modifications of dispersion dependences of the composite glass. For example; for $f = 0.1$, the refractive index varies between ~ 1.2 and 2.1 on the different sides of the SP resonance. Finally from the spectra in Fig. 11 (c) it can be seen that with an increase in volume filling factor there is an obvious increase in reflectivity of the composite material.

2.4.   Conclusion

This chapter briefly covered the properties of metallic nanoparticles and dielectric materials embedded with metallic nanoparticles with a focus on glass embedded with silver nanoparticles. An overview of Maxwell-Garnett theory was also provided as this method of effective medium theory will form the basis of the spectral analysis performed throughout the proceeding work.

This introduction to these materials is not intended to be comprehensive however aims to provide the necessary background for the proceeding chapters. More in depth reviews of the optical properties of nanostructured random media can be found in [12] and [28].

Chapter 3: On thermal poling of glass and glass embedded with silver nanoparticles

3.1. An introduction to thermal poling

Thermal poling has been extensively investigated as it has been shown to be a reliable and reproducible technique for inducing non-linear optical properties within glass [1-6]. Parallel plate thermal poling of glass involves sandwiching the glass between two electrodes and applying a dc electric field across the sample while at elevated temperatures. This forms subsurface layers that exhibit nonlinear optical properties (such as the generation of second harmonics) which are depleted of highly mobile positive ions, such as Na^+. During poling the applied electric field forces the positive ions to move from the near-anode region into the bulk of the material, towards the cathode [49-51]. Due to the reduction in ionic content in these near-surface layers there is a discrepancy in the refractive index of the glass where there has been contact with the anode. This variation in the refractive index has previously been exploited for the fabrication of waveguides [52, 53].

3.2. Thermal poling of pure glass

In this section the results of performing thermal poling on a sample of soda lime float glass are presented. It will be shown that a combination of applied voltage across the glass while it is in a moderately elevated temperature environment results in the displacement of the positive ions within the glass matrix. Firstly, the method

used for thermal poling of soda-lime float glass will be described before analysis of the sample will show that the positively charged ions within the glass have been successfully displaced.

Figure Fig. 12 shows a typical experimental arrangement for parallel plate thermal poling. For the poling of pure soda-lime float glass a sample was sandwiched between two pressed contact steel electrodes (rectangular, area of 100 mm^2). The sample was then placed inside the oven (Carbolite RWF) in air atmosphere before heating to a temperature of 553 K. Once the temperature had been allowed time to settle (~45 mins) a dc voltage of 0.1 kV was applied across the thickness of the samples using a high voltage source; F.u.G. Elektronik HCE 7-3500 POS. This power supply can supply voltages up to 6500V at currents up to 5mA and has a built in USB controller. Using this controller it was possible to control and monitor the functions of the power supply through a connected PC, this also allowed for the recording, plotting and saving of the data.
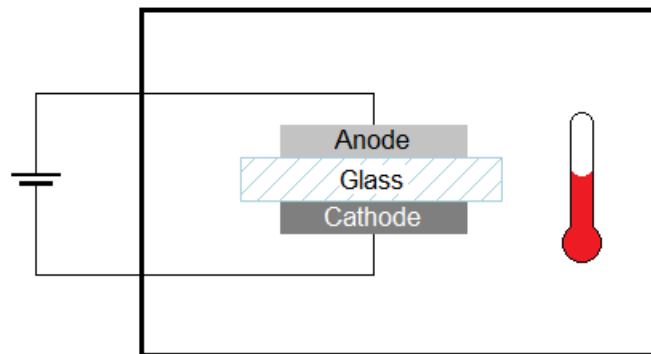
Fig. 12.Typical setup for the thermal poling of soda-lime float glass. Graphite is often inserted between the electrodes and the glass in order to provide a better contact between the materials and to accept any substances pushed out of the glass as a result of the poling procedure.

Once the current had been allowed to settle (~50 mins) the voltage was increased to 0.2 kV. The current was again allowed to settle before the applied voltage was increased to its maximum for this sample; 0.3 kV. The current was allowed to settle for a final time before the applied voltage was removed and the oven temperature allowed to decrease before the sample was withdrawn. The behaviour of the current over this period is illustrated in Fig. 13.

Since soda-lime glasses possess high ionic conductivity [54], it is important to take care in order to avoid electric breakdown of the material [4]. Here this was achieved by applying the voltage in small amplitude steps; for this sample 0.1 kV up to a value of 0.3 kV. By applying the voltage in this way the current never exceeded 30 µA throughout the period of the treatment, the total duration of which was ~150 mins. By integrating the current over the total time of the applied voltage the total charge transfer is calculated as 3.62 mA·s·cm^{-2} for this sample.
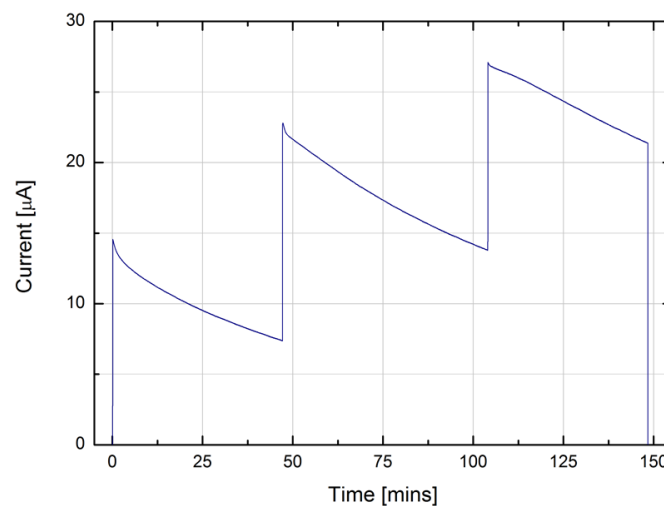
Fig. 13. The current-time dynamics recorded during the poling of soda-lime float glass. An initial voltage of 0.1 kV was applied and the current allowed to drop before the voltage was increased to 0.2 kV. This was repeated until the voltage had reached 0.3 kV. This step-wise application of the voltage was employed as a means of avoiding electronic breakdown of the glass [4].

In order to better understand the displacement of the positive ions by thermal poling the distribution of the key elements of the glass was measured by using X-ray element analysis, Fig. 14; this was performed using a Hitachi S-4700 field emission scanning electron microscope (SEM). The distribution of the pivotal elements; sodium, potassium and silicon, in a sample of pure soda-lime float glass was measured before and after thermal poling at 553 K to a maximum voltage of 0.3 kV (achieved in 0.1 kV steps).
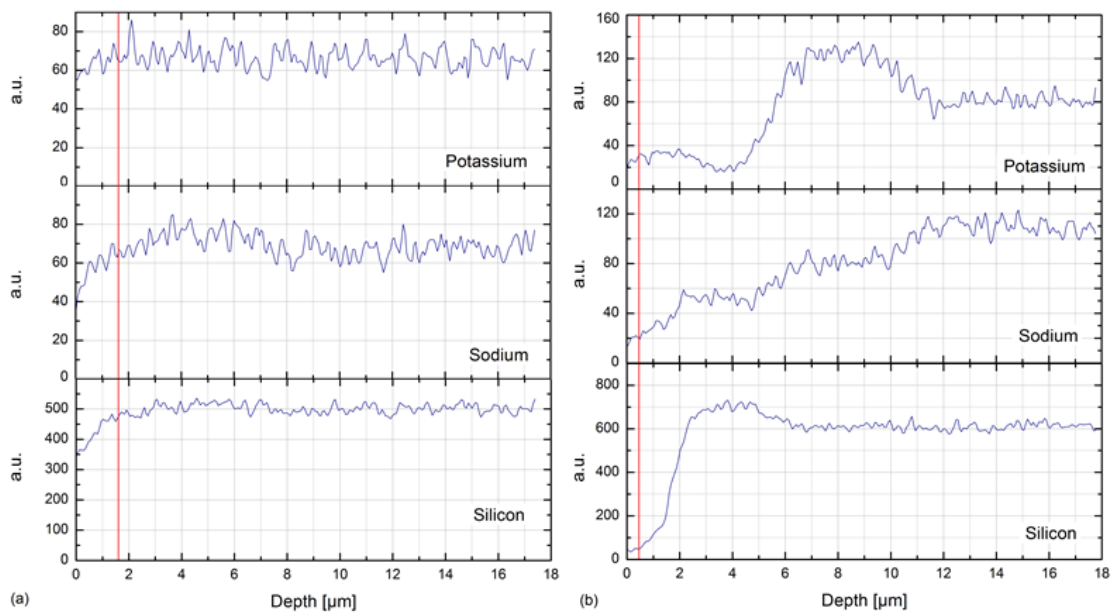
Fig. 14. The distributions of key elements (sodium, potassium and silicon) as a function of depth measured by local X-ray element analysis of vertical cross sections of pure soda-lime float glass (a) before and (b) after poling at a maximum applied voltage of 0.3 kV (applied in 0.1 kV steps). The red line indicates the surface of the glass.

Seen in Fig. 14 (and as previously reported in the literature [55, 56]) after poling the sodium and potassium content close to the glass surface has decreased, however increases at a depth of around 6 μm. It is not possible to distinguish between atoms and ions using SEM however it can be deduced that due to the application and direction of the electric field the changes in the distribution of these

key elements would be due to a field-driven displacement of Na+ and K+ ions. With this in mind it is a reasonable assumption to take the depth at which the Na and K concentration begins to increase as the thickness of the poled region and would hence be approximately 6 μm.

3.3.   Thermal poling of glass embedded with silver nanoparticles

This section will describe the results of thermal poling on glass embedded with silver nanoparticles, a process more commonly known as electric field assisted dissolution, EFAD. It will be shown that the application of an electric field at moderately elevated temperatures on this glass results in the dissolution of the silver nanoparticles into the bulk glass matrix. The method for this procedure will be described along with an analysis of the material post-poling.

Silver embedded glass samples were prepared from soda-lime float glass (72.5 SiO_2, 14.4 Na_2O, 0.7 K_2O, 6.1 CaO, 4.0 MgO, 1.5 Al_2O_3, 0.1 Fe_2O_3, 0.1 MnO, 0.4 SO_3 in wt%) by Ag^+-Na^+ ion exchange. For the ion exchange process the glass substrate was placed in a mixed melt of $AgNO_3$ and KNO_3 at 673 K [36]. Thermal annealing of the ion exchanged glass in H_2 reduction atmosphere (typically at 673 – 723 K) results in the formation of spherical silver nanoparticles. The samples used in this section contained spherical Ag nanoparticles, 30-40 nm in mean diameter, distributed in a thin surface layer approximately 6 μm thick on both sides of the glass (the total thickness of the glass plate was 1 mm). It was necessary for the experiment described that the samples have an embedded silver layer on only one surface of the glass. In order to achieve this, the silver layer was removed from one side of the glass samples by etching in 12% HF acid.

For the thermal poling of glass embedded with silver nanoparticles a similar setup is used as for that of pure glass mentioned in a previous section on thermal poling of pure glass. As before the sample was poled using the parallel plate thermal poling technique which required that the sample be placed in a sandwich configuration between two pressed contact steel electrodes (rectangular of area 100 mm^2), and inserted into an air atmosphere oven (Carbolite RWF). Unlike the thermal poling of pure glass, the configuration of the electrodes is important due to the presence of the nanoparticle containing layer. In order for dissolution of the silver nanoparticles to take place it is necessary that the silver containing layer faces towards the anode so that the current direction drives the silver ions into the bulk of the glass during the poling process, Fig. 15.
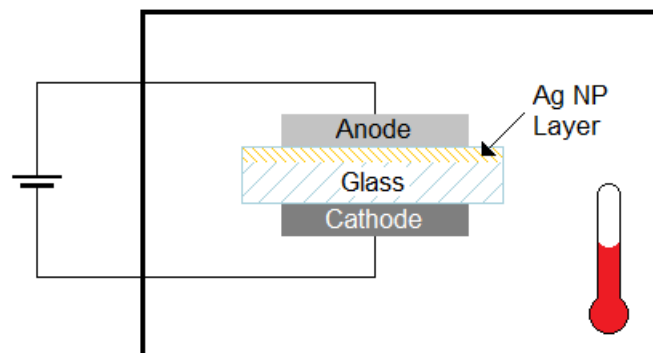
Fig. 15. Typical experimental arrangement for the thermal poling of glass embedded with silver nanoparticles or 'Electric Field Assisted Dissolution' (EFAD). Note the arrangement of the glass sample here; the silver containing layer faces toward the anode.

Once in the oven the sample was heated to 573 K and allowed time for the temperature to settle (~45 mins). A dc voltage of 1.0 kV was then applied across the sample using a high voltage source (F.u.G. Elektronik HCE 7-3500 POS). Due to the presence of silver nanoparticles; electronic breakdown of the material is less likely to occur and so there is no need to introduce a voltage in a step amplitude fashion as

was the case with the pure glass. Once the voltage had been applied the setup was allowed 25 hrs for the current to drop. This was in an attempt to completely remove any silver nanoparticles from the poled area. Fig. 16 (a) shows the current-time dynamics recorded during the poling procedure.
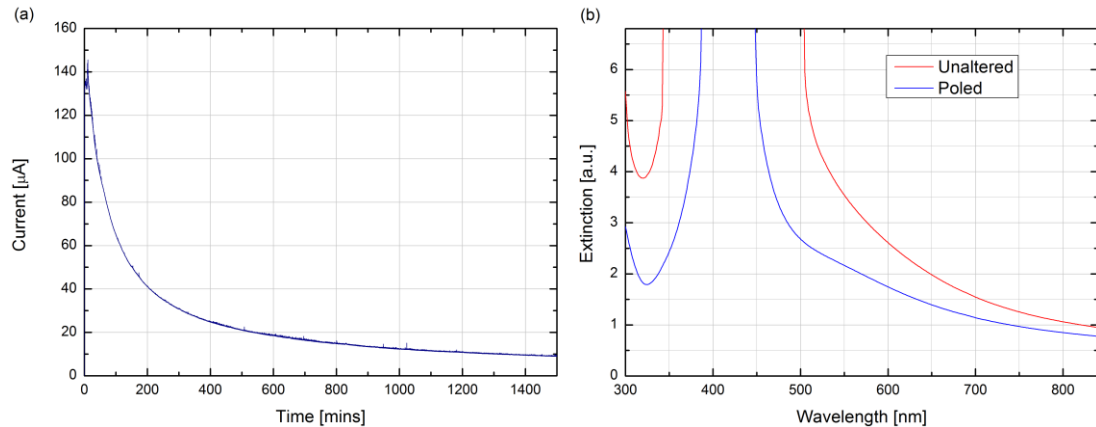
Fig. 16. (a) Current-time dynamics recorded for thermal poling of glass embedded with silver nanoparticles. This sample was poled in an oven temperature of 573 K using an applied electric potential of 1.0 kV. (b) The measured extinction spectra for this sample shown for before ('Unaltered') and after poling ('Poled').

The extinction spectra pre- and post-poling were measured and are compared in Fig. 16 (b). As can be seen from these results the poling has caused a perceived narrowing of the SPR band. Although on a saturated plot this could indicate an *actual* narrowing of the SPR or a decrease in the peak height both would be in agreement with Maxwell-Garnett theory [8, 28, 57-58] which predicts that a narrowing of the SPR band or a reduction in the SPR peak height is due to a reduction in the filling factor of the metal inclusions [8, 58]. Here this is owing to the dissolution of the nanoparticles into the glass matrix caused by the combined action of the applied electric field and increased local temperature [10, 11].

The result of thermal poling can be clearly seen with the naked eye; before dissolution the glass is a highly reflective yellow-brown colour due to the presence the silver nanoparticles, after thermal poling these nanoparticles have been dissolved into the glass matrix and therefore the glass loses some of its dense colour and is clearer, more like the original soda-lime float glass. This can be seen in Fig. 17.
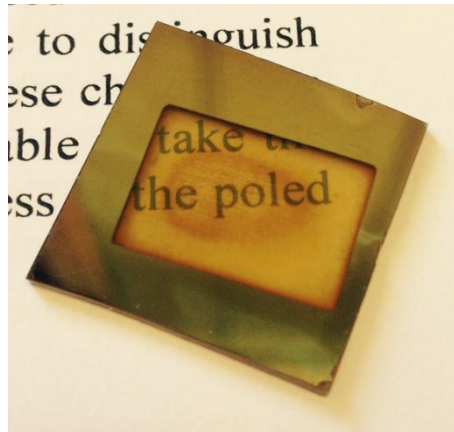
Fig. 17. Photograph taken of silver nanoparticle embedded glass after thermal poling (EFAD). The area which was in contact with the electrode during the experiment is easily recognisable as a rectangular transparent region in the centre of the opaque untouched glass. This is due to the dissolution of the silver nanoparticles within the glass matrix which takes place during poling and results in the processed area becoming clearer and less yellow than the original sample.

3.4.   Analysis of the conductivity of poled glass and poled glass embedded with silver nanoparticles

In order to get a better understanding of the effects of thermal poling on glass (both pure and embedded with silver nanoparticles) the conductivity of the glass was measured before and after poling. This would give insight into how the ionic content (i.e. charge carriers) was altered by the poling process.

In total four samples were prepared for the conductivity measurements; a sample of pure soda-lime float glass unaltered, a sample of glass embedded with silver nanoparticles also unaltered and a sample of each type of glass after poling. For the pure glass the poled sample was treated in an oven at 553 K using a maximum applied voltage of 0.3 kV (achieved in 0.1 kV steps) for ~250 mins. The silver embedded glass was thermally poled in an oven at 573 K using a constant voltage of 1.0 kV over 25 hours. This was done in an attempt to completely eradicate the poled area of any silver content.

Two gold electrodes in a gap-cell configuration (Fig. 18, width $w = 0.2$ cm, length $l = 0.7$ cm, separation $s = 0.1$ cm) were deposited on the surface of each sample using a thermal evaporation unit (Edwards model 307) operating at a base pressure of around 4×10^{-5} mbar.
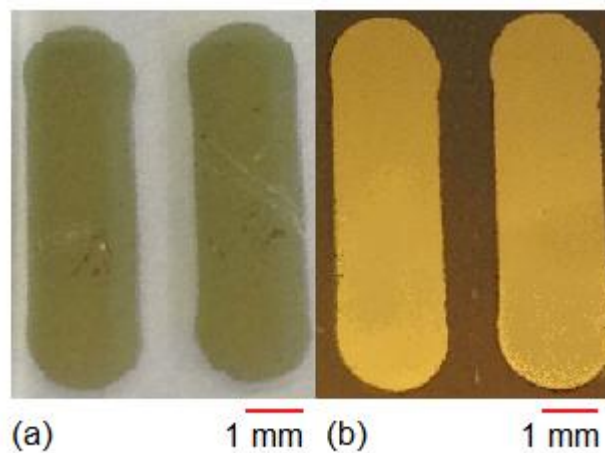
(a)   1 mm (b)   1 mm

Fig. 18. Photographs showing deposited gold electrodes on (a) a sample of unaltered soda-lime float glass and (b) an unaltered sample of glass embedded with silver nanoparticles. Due to some slight damage (visible in photographs) these were not the electrodes used for the measurements; however electrodes deposited in the same manner were used and these images serve to show how these appeared on the glass samples.

The electrical resistance (R) of the samples was then determined by performing current-voltage measurements using a source-measurement unit (Keithley Model 236). Resistance data was obtained for temperatures (T) ranging from 335 K to 455 K by attaching samples to a ceramic heating element in a sealed air enclosure. The gap-cell current response over this temperature range exhibited excellent Ohmic behaviour for applied voltages up to 100 V which allowed for the associated conductivity (σ) for samples of thickness $d = 1$ cm to be calculated as;

$$\sigma = \frac{1}{R}\left(\frac{d}{wl}\right).$$

22

Conductivity data were generally recorded as the sample temperature was reduced following an initial short annealing period at 455 K to remove any surface contamination such as water-vapour. Good reproducibility of $\sigma(T)$ sample data was observed following this procedure.

The conductivity, calculated according to Eq. 22, for each sample is plotted in Fig. 19 from which it is observed that over the experimentally accessible temperature range σ exhibits Arrhenius behaviour according to;

$$\sigma = \sigma_0 \exp\left[-\frac{\Delta E}{k_B T}\right].$$

23

In Eq. 23; k_B is the Boltzmann constant and σ_0 and ΔE respectively represent a pre-exponential conductivity factor and activation energy that are characteristic of the ionic transport mechanism within the glass.
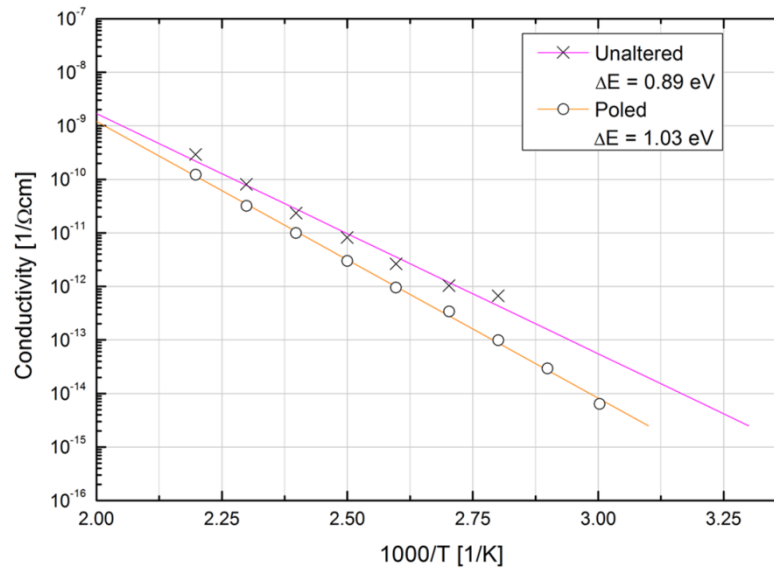
Fig. 19. Comparison of the conductivity of unaltered soda-lime float glass ("Unaltered") and a sample post poling ("Poled"). The post poling sample was thermally poled in an oven at 553 K using a maximum applied voltage of 0.5 kV (achieved in 0.1 kV steps).

Fig. 19 shows a comparison of the unaltered and poled samples of pure glass. From this image it is evident that poling results in a decrease in the conductivity of the glass compared to its original state. This reduction in conductivity is accompanied by a systematic increase in the associated *activation energy* of the glass, from 0.89 eV to 1.03 eV, meaning that the energy required for conductivity has increased.

After poling the deficit of positive charge caused by the displacement of the positive ions by the poling process is compensated by hydronium ions (H_3O^+) which are formed on the surface from the ambient air [59, 60]. The mobility of H_3O^+ ions is much lower than the alkali ions (sodium, potassium) from the glass and as the conductivity of the glass is proportional to the mobility of positive ions it is subsequently reduced post-poling.
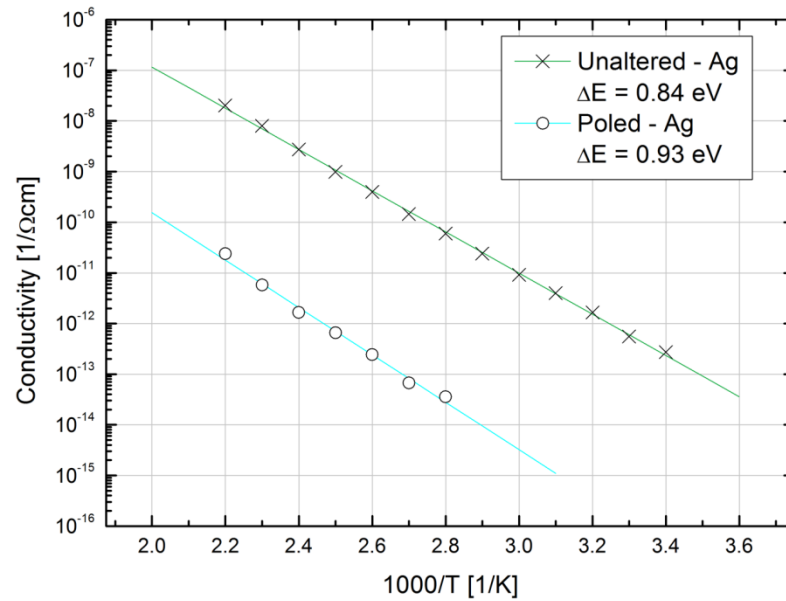
Fig. 20. Plot showing the difference in conductivity of unaltered glass embedded with silver nanoparticles ("Unaltered - Ag") and a sample after thermal poling ("Poled - Ag") at 553 K using a maximum applied voltage of 0.5 kV (achieved in 0.1 kV steps).

Similarly, there is a notable decrease in the conductivity of glass embedded with silver nanoparticles after thermal poling. However in this instance the decrease in the conductivity is due to the dissolution of silver particles with the glass. The silver nanoparticles, now in their ionic state, are no longer able to act as positive charge carriers and thus accounts for this decrease in conductivity. Again, lowered conductivity is accompanied by an increase in the associated activation energy of the glass, from 0.89 eV to 0.93 eV.

3.5.   Summary

This chapter aimed to give an insight into the thermal poling of glass (both pure and embedded with silver nanoparticles) which will be essential for the proceeding chapters. To begin an overview of the process of thermal poling was

described; detailing how an applied electric field and moderately elevated temperatures causes displacement of positive ions within glass.

The thermal poling process was then demonstrated using 'pure' soda-lime float glass. Using the relatively simple technique described it was shown using X-ray element analysis that after thermal poling the distribution of positive ions (mainly sodium and potassium) had decreased close to the surface of the glass.

The next section investigated how thermal poling in glass embedded with silver nanoparticles differs to that of the pure glass. It was described how this process, more commonly known as EFAD, although similar in procedure to thermal poling varies fundamentally in that it does not involve the displacement of positive ions from the glass matrix but instead relies upon the dissolution of silver nanoparticles.

The EFAD process was then illustrated with a sample of glass embedded with silver nanoparticles. Immediately after poling of the silver-doped glass the dissolution is visible by eye. The dissolution is backed up by Maxwell-Garnett theory which states that a narrowing of the SPR band is indicative of a decrease in the metal filling factor of such a composite material.

To further analyse the effect poling has on both the pure glass and the glass embedded with silver nanoparticles the conductivity of the glasses was measured before and after poling. The results showed that post-poling both types of glasses had a significant decrease in conductivity owing to the decrease in available positive charge carriers (sodium and potassium for the pure glass and silver for the metal embedded glass).

Utilising what was shown in this chapter, the following two chapters will use the relatively simple thermal poling process in order to fabricate functional diffraction gratings.

Chapter 4: Imprinting of pure glass

4.1.   Introduction

This chapter will describe the process for fabricating a diffractive optical element, DOE, in soda-lime float glass using the thermal poling process. Just as described in the previous chapter the glass is sandwiched between two electrodes; a flat metal cathode as before, however in order to create the structuring necessary for the DOE a metallic mesh is used as the anode. We will discuss how applying a direct current, while at a moderately elevated temperature of 553 K, induces thermal poling of the glass but most notably the result that the structured pattern of the anode is imprinted within the glass as the electric field causes ion depleted regions where there is contact between the glass and electrode.

The current-time dynamics of the structuring process, conductivity measurements, optical analysis, atomic force microscopy and resultant diffraction patterns of samples from this fabrication process are presented.

4.2.   Experimental

Soda-lime float glass (72.2 SiO_2, 14.2 Na_2O, 0.71 K_2O, 6.5 CaO, 4.42 MgO, 1.49 Al_2O_3, 0.13 Fe_2O_3, 0.4 SO_3, in wt.-%) was employed for the fabrication of the DOEs. As in Fig. 21, 1 mm thick samples of this glass were sandwiched between two metallic electrodes.
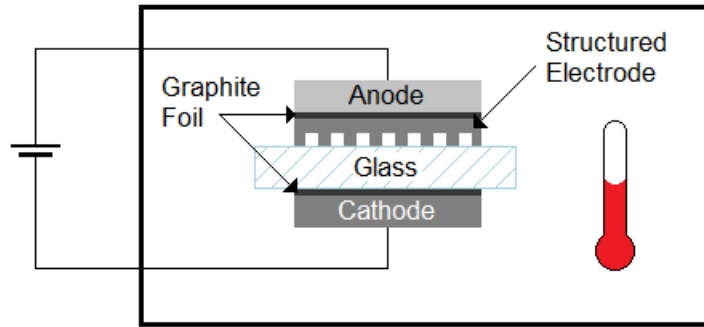
Fig. 21. A schematic illustration the setup used for the structured thermal poling of soda-lime float glass. A metallic mesh acts as the anode, imprinting a pattern of ion depleted regions which mirror the pattern of the mesh.

The notable exception for these experiments compared to the plain poling described in the preceding chapter is that the flat metallic plate previously used as the anode has been replaced with a periodically structured silicon electrode with a lattice constant of 2 μm, Fig. 22.

The structured electrode, fabricated by the Max Planck Institute for Microstructure Physics at Halle, Germany [9]85; was grown in a photoelectrochemical etching process of lithographically prestructured <100>-oriented n-type silicon wafers. In each case, the front side of the wafer was in contact with hydrofluoric acid (HF; cHF = 5 wt.-%; T = 10 °C) whereas the backside was illuminated generating electron–hole pairs. An external anodic bias then consumed the electrons, and the electrons/holes diffused through the whole wafer to the silicon electrolyte interface, promoting the silicon dissolution there. The pores with very flat surfaces and high aspect ratios grew straight along the (001) direction of the silicon single crystal [61, 62]. The macroporous silicon samples had a lattice constant of 2 μm and before use were sputtered with 10 nm chromium film to avoid anodic bonding during the experiments [63, 64].

The cathode was a flat piece of stainless steel (rectangular, area = 1 cm^2). In order to improve the contact between the glass and the electrode a piece of graphite sheet was inserted between the sample and the cathode, similarly between the positive electrode and the metallic mesh. An added advantage of having graphite at the negative electrode is that the substances coming out of the glass do not pollute the electrodes. Additionally, graphite forms a non-blocking cathode since it accepts alkali ions.
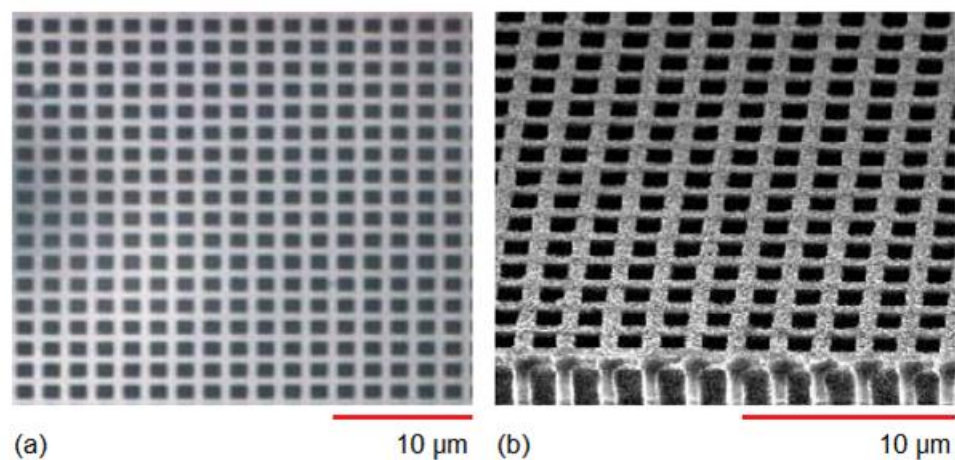
Fig. 22. (a) Microscope image and (b) an SEM image taken of the surface of the periodically structured silicon used as the anode in the imprinting of soda-lime float glass. The lattice constant of the structured silicon is 2 μm with the hole having a width of approximately 1 μm.

The samples were then placed in an air atmosphere oven (Carbolite RWF) and the electrodes were connected to a high-voltage power supply (F.u.G. Elektronik HCE 7-3500 POS). For all samples the oven temperature was kept constant at 553 K (an hour at this temperature was allowed before applying the dc voltage in order to ensure the temperature had settled) while the effect of using a different peak voltage was investigated by changing the peak applied dc voltage for each sample. For all samples the voltage was applied in small amplitude steps, either 0.2 kV or 0.1 kV, in

a way that during each step the current never exceeded a few hundred microamperes, typically <150 μA. This was done in order to avoid electric breakdown of the material.

The characterizations of the samples were performed using a KEYENCE Digital Microscope VHX-1000, JEOL JSM-7400F scanning electron microscope and a He-Ne laser.

4.3. Results and Discussions

In order to determine what parameters produced more efficient diffraction gratings; four samples were thermally poled to different maximum voltages however still using the same step-up voltage technique described earlier in order to avoid electronic breakdown of the material.

Post poling all samples exhibited clear structured patterns with a lattice constant of 2 m when viewed under the microscope, images taken can be seen in Fig. 23. This is in agreement with the lattice constant and pattern of the structured electrode used as the anode (Fig. 23 (i)) implying that the pattern of the anode has been imprinted onto the surface of the glass.
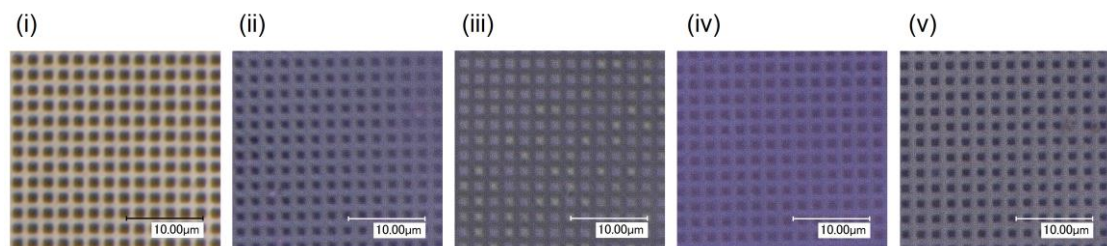
Fig. 23. Microscope image taken of (i) the surface of the structured electrode and the glass sample surfaces post poling at a maximum voltage of (ii) 1.0kV (in 0.2 kV steps), (ii) 0.8 kV (in 0.2 kV steps), (iii) 0.6 kV (in 0.2 kV steps) and (v) 0.3 kV (in 0.1 kV steps).

Described in the chapter on thermal poling; the structures shown in the microscope images are formed due to the migration of highly mobile positive ions (namely Na^+ and K^+). These ions are mobile at the elevated temperature used during the experiment and are driven away from the positive electrode by the electric field. As before some of these positive ions are pushed into the bulk of the material however in this case due to the structure of the electrode they may also be directed into the relief areas where the glass is not in contact with the electrode (Fig. 24 illustrates the displacement of the ions). It is these areas of relief which appear as squares in the microscope images and form the structures seen in Fig. 23. The grid structure, i.e. depletion regions, are a few micrometres thick [65] and, due to the reduced ionic content, have a lower refractive index that the 'relief' structures.
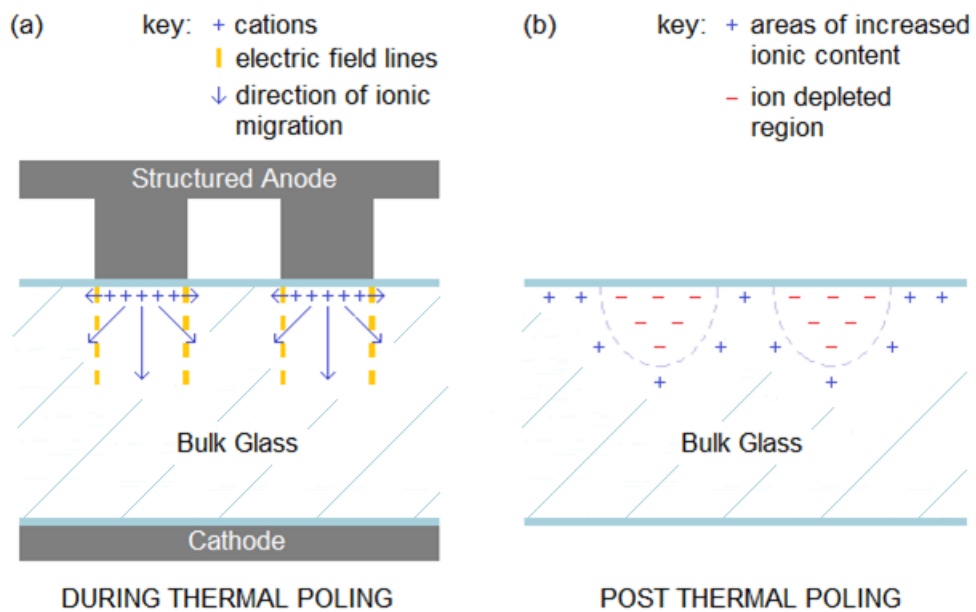
Fig. 24. (a) Schematic illustrating a sample of pure soda-lime float glass during thermal poling with a structured electrode. Positive ions are shown being driven into the bulk glass and relief regions (areas not in contact with the electrode) by the electric field. (Note: the electric field lines are essentially parallel over the relatively small

depth of the ion depletion region.) (b) Post thermal poling there are now areas of increased ionic content in the relief regions of the glass and ion depleted regions where there had been contact with the electrode.

Investigation of the ion displacement was performed by measuring the surface conductivity of structured thermally poled glass and comparing to those for the unaltered sample and the thermally poled sample produced using the plain electrode from chapter 3. The aim of this is to show that thermal poling using the structured electrode will provide displacement of the cations only where there is contact between the glass surface and the electrode and thus not provide the maximum poling available from full contact as in the sample poled using the plain electrode.

The conductivity was calculated following the same method described in chapter 3 and Fig. 25 shows the conductivity of the sample poled with the structured electrode ("Grid Structured") alongside that of the unaltered soda-lime glass ("Unaltered") and the thermally poled sample using the plain electrode ("Plain Poled").
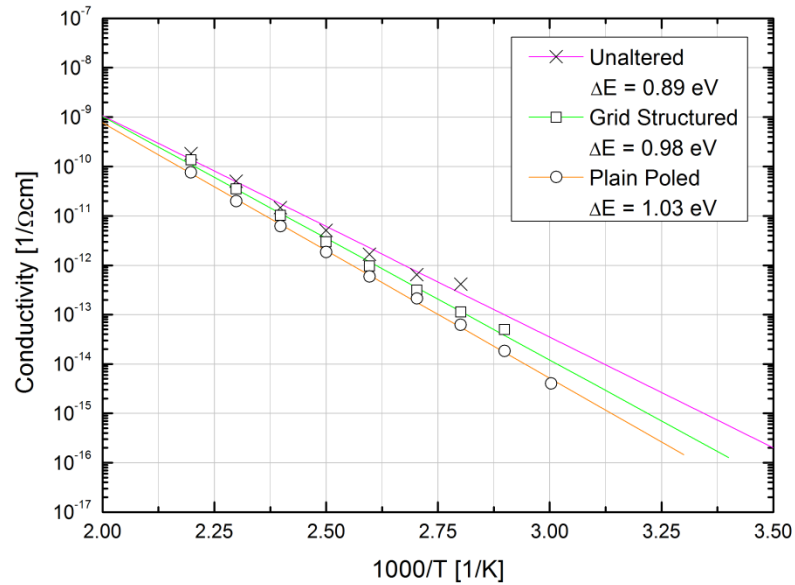
Fig. 25. A comparison of the conductivity of the grid-structured thermally poled glass ("Grid Structured") to that of the unaltered soda-lime glass ("Unaltered") and the plain electrode thermally poled sample from the previous chapter ("Plain Poled"). Both of the modified samples were poled under the same conditions (air atmosphere oven at 553 K with a maximum voltage of 0.3 kV achieved in steps of 0.1 kV). The solid lines on the plot show the best fit of Eq. 23 to the data points shown, the values calculated for ΔE for each sample are given in the key.

The activation energy was lowest for the unaltered glass sample, 0.89 eV, and increased post poling; this is because the activation energy is indirectly proportional to ion mobility and as the positive ions from the glass are replaced with lower mobility H_3O^+ ions the activation energy increases. After grid structured poling the absence of high mobility charge carriers can be seen as the activation energy increases to 0.98 eV and when the maximum number of these highly mobile positive ions has been driven into the bulk glass, during plain electrode poling, the activation energy has increased further to 1.03 eV. As grid structured poling only selectively displaces the positive ions within the glass, some high mobility ions still

remain, while a maximum number of these ions have been replaced by using the plain electrode and hence this procedure produces the lowest conductivity.

The current-time dynamics were recorded for the durations of the experiments on all four samples and are shown in Fig. 26. The first sample was poled to a maximum voltage of 1.0 kV (Fig. 26 (a)) by initially applying a voltage of 0.2 kV causing a current peak of ~60 μA which decreases, following an exponential-type curve, below ~20 μA within 40 min, A second voltage step was then applied inducing a current peak of ~105 μA which was again allowed to drop to ~30 μA following a similar exponential-like curve, before the third voltage step was applied. The voltage was increased following this pattern of allowing the current to drop before applying an additional 0.1 kV. The current reached a maximum of ~115 μA after each increase and followed a similar decreasing curve to a minimum of approximately 30 μA.
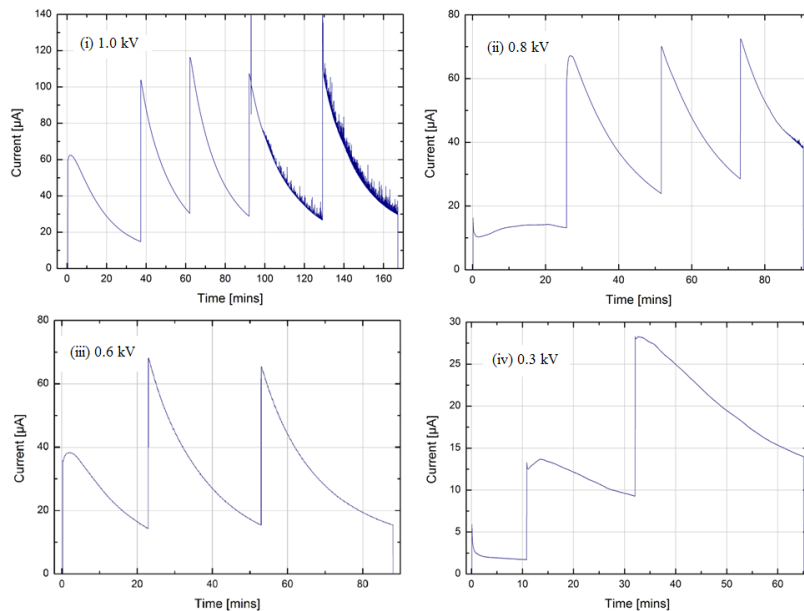
Fig. 26. The current time dynamics recorded during the structured thermal poling of 'pure' soda-lime float glass. The maximum applied electric potential; (i) 1.0 kV (in 0.2 kV steps), (ii) 0.8 kV (in 0.2 kV steps), (iii) 0.6 kV (in 0.2 kV steps) and (iv) 0.3 kV (in 0.1 kV steps).

The total charge transfer for the procedure was calculated by integrating the current over the total time the voltage was applied for and gives a total charge transfer of 0.18 A·s·cm^{-2} for the sample poled with a maximum voltage of 1.0 kV.

As can be seen for Fig. 26 (ii), (iii) and (iv) the current-time dynamics for the other samples followed a similar trajectory; with the first current peak being significantly lower than those for the proceeding voltage increase steps.

The total charge transfer for each sample decreased with decreasing maximum voltage as would be expected. The total charge transfer for the modified samples is documented in Table 1.

Table 1. Details of the modified soda-lime float glass samples. All samples were thermally poled in an air atmosphere oven at 553 K.

Maximum voltage used during poling (kV)	Voltage step increase (kV)	Sample area (cm^2)	Total charge transfer (A·s·cm^2)
1.0	0.2	3.04	0.18
0.8	0.2	1.65	0.12
0.6	0.2	1.76	0.09
0.3	0.1	1.54	0.04

All four samples functioned, with varying degrees of efficiency, as diffractive optical elements; the diffraction pattern for each sample can be seen in Fig. 27. Comparing these patterns for the different samples shows a variation in the intensity of the diffraction patterns and in the number of orders that are clearly visible, the first and second orders were certainly visible for all four samples.
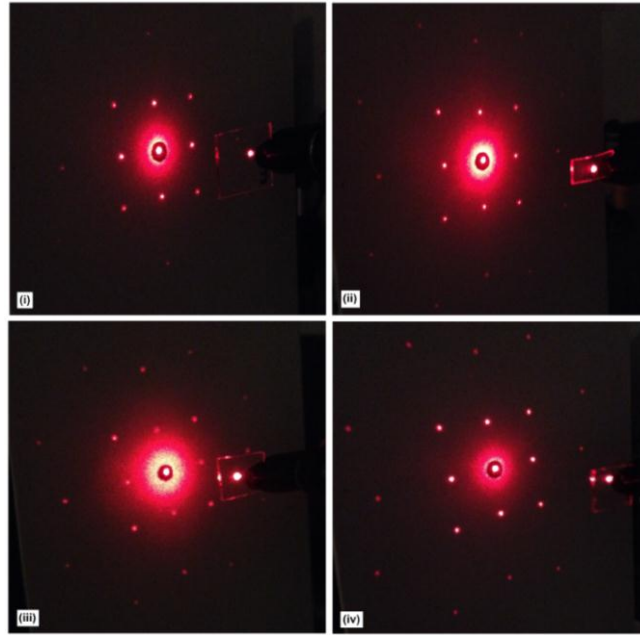
Fig. 27. The diffraction patterns (in transmission) of the samples thermally poled using a structured electrode to a maximum voltage of; (i) 1.0 kV (in 0.2 kV steps), (ii) 0.8 kV (in 0.2 kV steps), (iii) 0.6 kV (in 0.2 kV steps) and (iv) 0.3 kV (in 0.1 kV steps). In order to take clearer images the intensity of the zero order was reduced by using a small piece of black felt.

The variation in intensity of the diffraction patterns was investigated by calculating the diffraction efficiency of each of the samples using Eq. 24;

$$\eta = P/P_0 \, , \qquad\qquad 24$$

where P_0 is the incident optical power and P is the power of the diffracted light. The calculated diffraction efficiencies are plotted in Fig. 28.
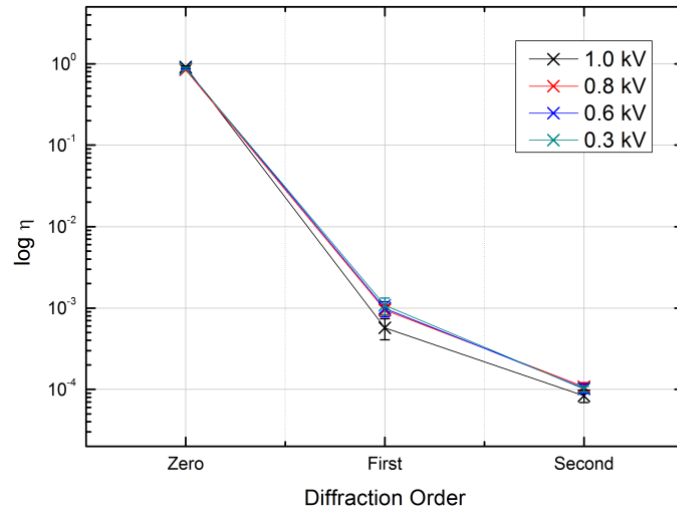
Fig. 28. Log plot displaying the values of diffraction efficiency (η) for the four structured thermally poled samples. The diffraction efficiency values are shown for the three most visible orders; zero, first and second, and were determined by using a 632 nm He-Ne laser. The key relates to the maximum applied voltage used (all voltages were applied in 0.2 kV steps bar the 0.3 kV sample for which the maximum voltage was achieved in 0.1 kV steps).

From these results it was determined that the sample with the lowest diffraction efficiency was produced using a maximum voltage of 1.0 kV, while the sample with the highest diffraction efficiency was fabricated using the lowest maximum applied voltage; 0.3 kV.

The height of the structures was subsequently investigated using atomic force microscopy (AFM) by tracing the surface profile; the results of which are shown in Fig. 29. The highest measured value for surface relief height was ~30 nm for the sample poled at a maximum voltage of 0.6 kV while the smallest structures were recorded as ~7 nm and produced when the maximum voltage was 0.3 kV. The relief height is proportional to the exposure time which was the longest for the sample poled at a maximum voltage of 1.0 kV and shortest for the sample poled at a

maximum voltage of 0.3 kV indicating that exposure time is not the only factor determining the height of the relief structures.
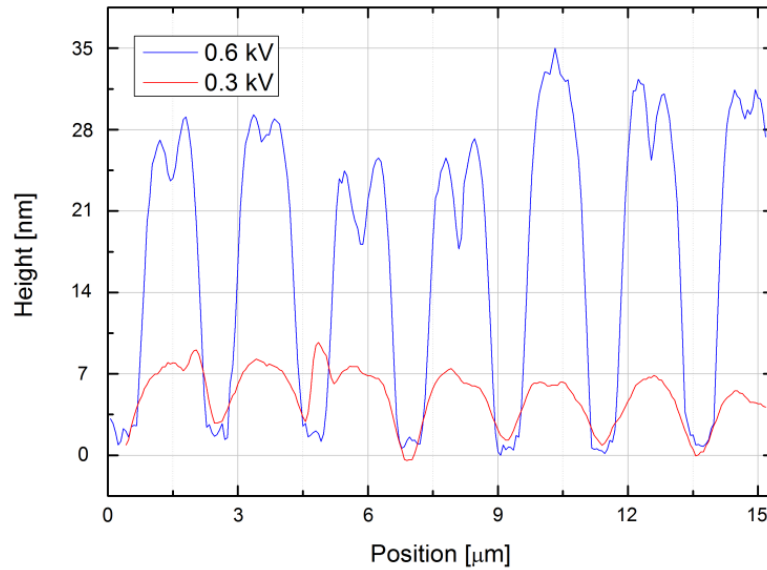
Fig. 29. Surface relief height of samples post structured thermal poling to a maximum voltage of; (i) 1.0 kV (in 0.2 kV steps), (ii) 0.8 kV (in 0.2 kV), (iii) 0.6 kV (in 0.2 kV steps), and (iv) 0.3 kV (in 0.1 kV steps).

Higher voltage increases the electric field strength between the two plates and at the edge of the areas of glass in contact with the electrode. With increased electric field strength the mobility of the hydronium ions increases resulting in increase in the depth profile of the structures and a smearing of the lateral surface profile [60]. The smearing of the surface profile results in a decrease in the phase modulation index and therefore with increased voltage the diffraction efficiency decreases. It is worth mentioning that the formation of surface reliefs and their heights as a result of thermal poling would also influence the diffraction efficiency.

The total poling time also affects the depth of the depleted region of positive ions within the glass [3]. As the poling time was dictated by the maximum voltage used, samples with a higher maximum voltage were poled for a longer time and therefore will have thicker depleted layers.

Using the parameters used to achieve the highest diffraction efficiency, 0.3 kV in 0.1 kV steps, a more complex pattern was attempted. In order to achieve this a sample of the same soda-lime float glass was thermally poled at 553 K applying the voltage in 0.1 kV steps to a maximum voltage of 0.3 kV using the grid structured electrode used earlier (Fig. 23 (i)). The experiment was then repeated exactly however this time placing the structured electrode at a 45° angle to its position in the original poling. By repeating the poling at different angles a star-like diffraction pattern was successfully produced and can be seen in Fig. 30.
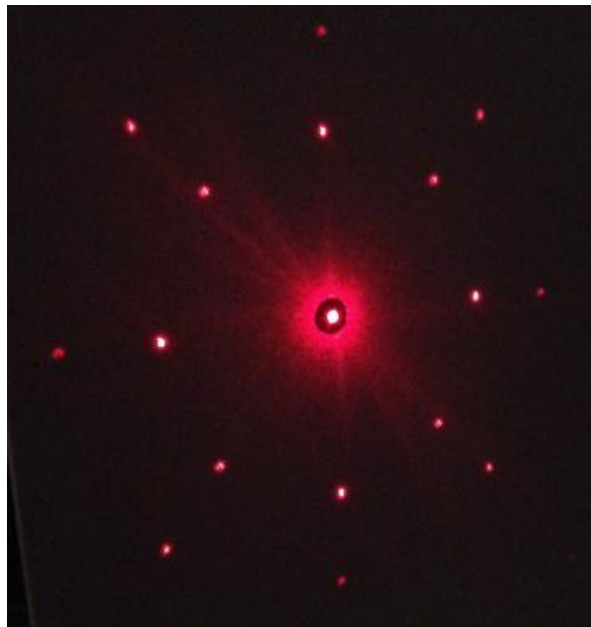
Fig. 30. The diffraction pattern of a sample of soda-lime float glass poled twice using a structured electrode at a different angle for each exposure; the effect is the star-like diffraction pattern seen. (The intensity of the zero order has been reduced for the photograph by using a piece of black felt).

4.4. Summary

Four samples of "pure" soda-lime float glass were poled to different maximum voltages using a grid structured electrode. The result was the fabrication of effective diffraction gratings with varying degrees of diffraction efficiency.

By comparison of the conductivity measurements of the grid structured sample to those of the unaltered and the plain poled samples of the previous chapter it was shown that the fabrication method results in the re-structuring of the glass itself and therefore its refractive index. However in this instance the presence of the structured electrode allows for the selective re-structuring of the glass and hence the refractive index varies periodically throughout the modified sample. It is believed that this variation in refractive index or the change in the surface profile due to the thermal poling process or indeed a combination of the two is responsible for the resultant diffraction pattern shown. As this process alters the structure of the glass itself and is not a coating or etching of the surface this process makes for much more robust and resilient diffractive optical elements.

The effectiveness of the diffraction gratings was then assessed by calculating the diffraction efficiencies of the fabricated samples. The results showed that the sample modified at a maximum voltage of 0.3 kV produced the most effective DOE and it was therefore these parameters that were used in order to produce a more complex pattern by double poling at different angles. This demonstrates that the diffraction pattern produced is governed by the electrode used and so complex, large-scale patterns can be easily fabricated using this process.

Chapter 5: Imprinting of glass embedded with silver nanoparticles

5.1. Introduction

In this chapter the knowledge from the two previous chapters will be combined in order to fabricate effective diffractive optical elements, DOEs, in glass embedded with *silver nanoparticles*. This will be done using the electric field assisted dissolution process described in chapter 4 however the anode will be replaced, as in the previous chapter, with a grid structured electrode of macroporous silicon.

The importance of the process parameters, the applied voltage and temperature, are investigated by analysis of the current-time dynamics of the structuring process, conductivity measurements before and after modification of the samples, SEM images of the structures produced, optical analysis of the fabricated samples and of course the resultant diffraction patterns of samples from this fabrication process are presented.

5.2. Experimental

Three pieces of 1 mm thick soda-lime float glass embedded with spherical silver nanoparticles were used in the experiments. The silver nanoparticles were of a mean diameter of 30-40 nm in a thin surface layer of ~6 μm on one side of the glass (prepared in the same manner as discussed on page 29), Fig. 31.
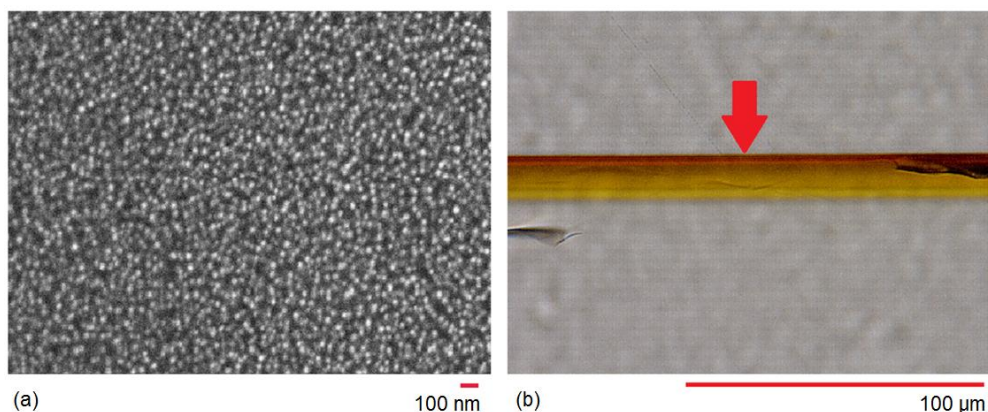
Fig. 31. (a) SEM image of the glass embedded with silver nanoparticles (seen as white spots) before EFAD along with (b) an image of a thin slice of the sample showing a cross section of the nanoparticle containing layer (the red arrow indicates the surface of the glass). As can be seen the volume filling factor of the layer reduces to zero within a few microns.

Each sample was placed in a sandwich-like configuration between two metallic electrodes in such a way that the remaining silver containing layer was facing the anode. The cathode was a piece of flat stainless steel (rectangular, area = 1 cm^2). The anode used was the same piece of structured macroporous silicon discussed in the previous chapter (page 40).

Graphite was used between the electrodes and the samples; acting as a non-blocking cathode protecting the electrode from the pollutants expelled by the glass during the experiment and providing a better contact between the glass and the electrodes. A schematic illustrating the configuration of the setup can be seen in Fig. 32.
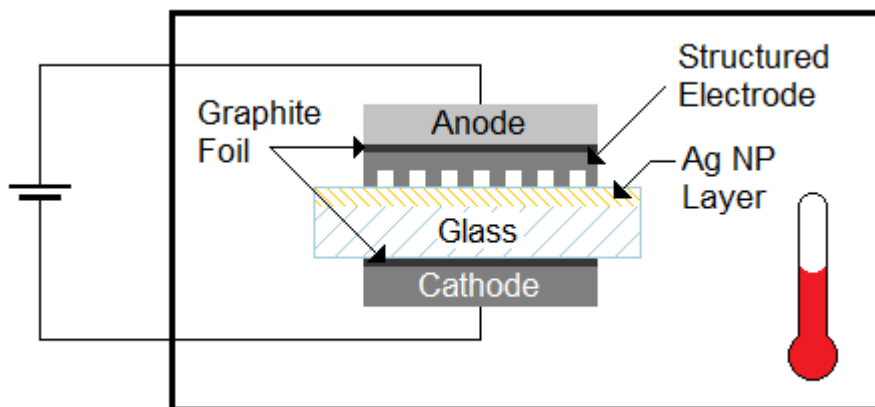
Fig. 32. An illustration of the setup used in order to fabricate effective DOEs in glass embedded with silver nanoparticles. Note the silver containing layer facing the structured electrode.

The samples were then placed in an air atmosphere oven and the electrodes were connected to a high-voltage power supply (F.u.G. Elektronik HCE 7-3500 POS). The exposure time for the samples was kept constant at 30 mins however the three samples were treated to three different conditions: (i) 0.6 kV at 473 K, (ii) 0.4 kV at 473 K and (iii) 0.4 kV at 573 K in order to investigate the effect of temperature and applied voltage on the effectiveness of the DOEs produced.

5.3.   Results and Discussions

The characterizations of the sample were performed using a JASCO V-670 UV/VIS/NIR Spectrophotometer, KEYENCE Digital Microscope VHX-1000, JEOL JSM-7400F scanning electron microscope and a He-Ne laser.

From the digital microscope images shown in Fig. 33; it can be seen that the experiments produced structuring with varying degrees of effectiveness. There is a visible variance in the colouring of the samples under microscope; this is due to uneven contact between the anode and the glass creating structures of varying height which causes a discrepancy in the colour observed at this level. Certainly these

images show structures within the glass with a measurable lattice constant of 2 μm which is in accordance with the grid pattern of the structured electrode used and indicates that successful imprinting of the electrode pattern has taken place.
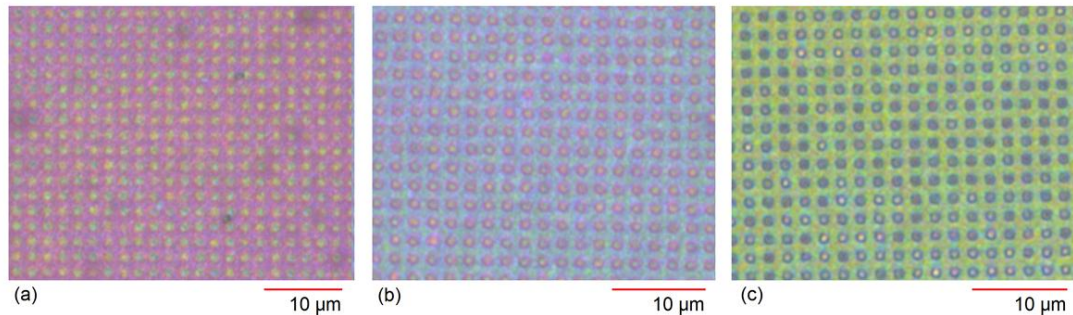
Fig. 33. Digital microscope images taken of the glass composite samples post-structuring at (a) (0.4 kV, 573 K), (b) (0.4 kV, 473 K), and (c) (0.6 kV, 473 K). The colour shift across the samples is due to different degrees of contact between the glass surface and the electrode which causes a variation in the height of the glass structures produced during poling. Each sample has a lattice constant of 2 μm matching that of the structured electrode used.

The structures are formed by the selective dissolution of silver nanoparticles within the glass. As described earlier the electric field assisted dissolution technique causes the breakdown of the silver nanoparticles, however, as the experiments described here use a structured electrode with a periodic pattern (unlike that of the plain electrode used earlier) where there is no contact between the glass and the electrode dissolution cannot take place leaving a grid pattern of structures consisting of unaltered silver nanoparticles surrounded by areas of dissolution which were in contact with the electrode.

In order to further analyse the effect of this selective dissolution of the nanoparticles the extinction spectra of the original sample of glass embedded with

silver nanoparticles was compared to that of the post EFAD samples, both the plain and the grid structured, Fig. 34.
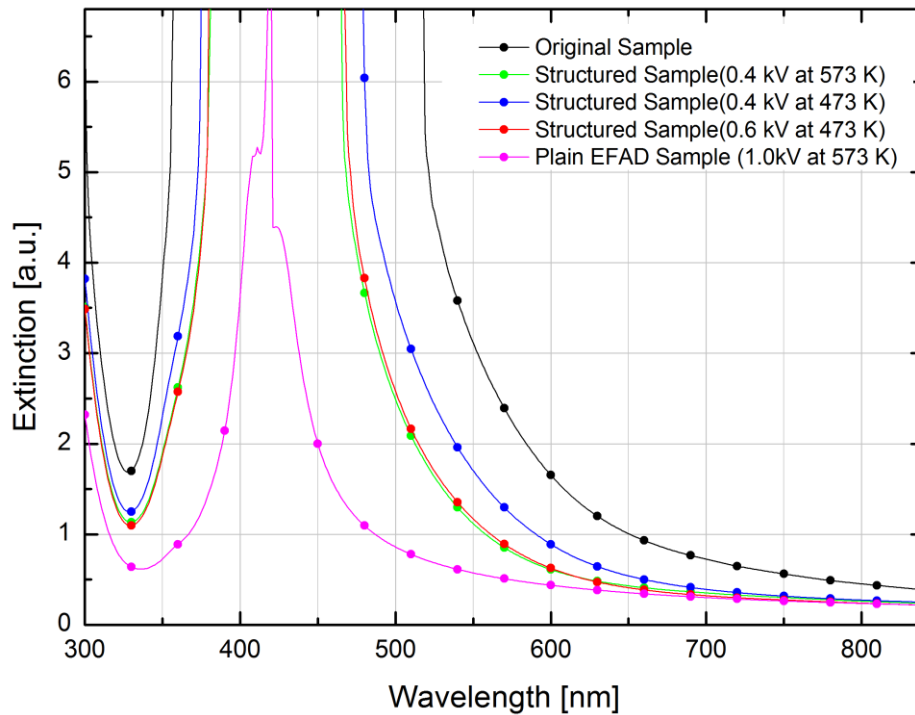
Fig. 34. Measured extinction spectra of the original sample of glass embedded with silver nanoparticles (black line) and samples after EFAD using a grid patterned structured electrode. Shown for reference; the extinction spectra for a sample after EFAD using a plain electrode (pink line) where a high level of dissolution had been achieved.

From this spectra it can be seen that the original sample of silver doped nanocomposite glass shows a strong and broad SPR band corresponding to the high volume filling factor of the embedded silver nanoparticles. For saturated spectra, an *apparently* narrower SPR band post EFAD could indicate either a *truly* narrower band, or a reduction in the SPR peak height that makes the SPR band *appear* narrower, or *both* effects could occur simultaneously. A simultaneous reduction is predicted by Maxwell-Garnett effective medium theory [8, 28, 57-58]. The theory predicts that a narrowing of the SPR band or a reduction in the peak height would be

indicative of a reduction in the volume filling factor of the inclusions [8, 66]. The reduction in filling factor is in accordance with the theory of EFAD which predicts the dissolution of the nanoparticles in the glass matrix owing to the combined action of the applied electric field and elevated temperature. The measured extinction spectra for the EFAD sample using the plain electrode has a more obvious narrowing of the SPR band for this reason; the greater electrode surface area in contact with the glass has initiated a greater dissolution of silver nanoparticles and thus a greater decrease in the volume filling factor of the inclusions than that of the structured samples.

Fig. 34 also shows that the structured samples at (0.4 kV, 573 K) and (0.6 kV, 473 K) are approximately the same in terms of the effect of the SPR band shape and position compared to that of the original sample whereas the sample produced at (0.4 kV, 473 K) does not have as notable an effect indicating that these parameters resulted in less dissolution of the silver nanoparticles.

Current as a function of time during the dissolution processes and its effect on the structuring are shown in Fig. 35. As can be seen from Fig. 35 (a), for the sample modified at (0.4 kV, 573 K), the current starts at ~ 3500 μA and then reduces exponentially below 100 μA within 10 min and then falls to zero within 30 min. Integrating the current over time gives a total charge transfer of ~ 0.13 A·s·cm^{-2}. This resulted in the formation of the structures shown in Fig. 36 (a) illustrated by SEM. The structures are ~500 nm high and formed some 500 nm beneath the surface of the glass.
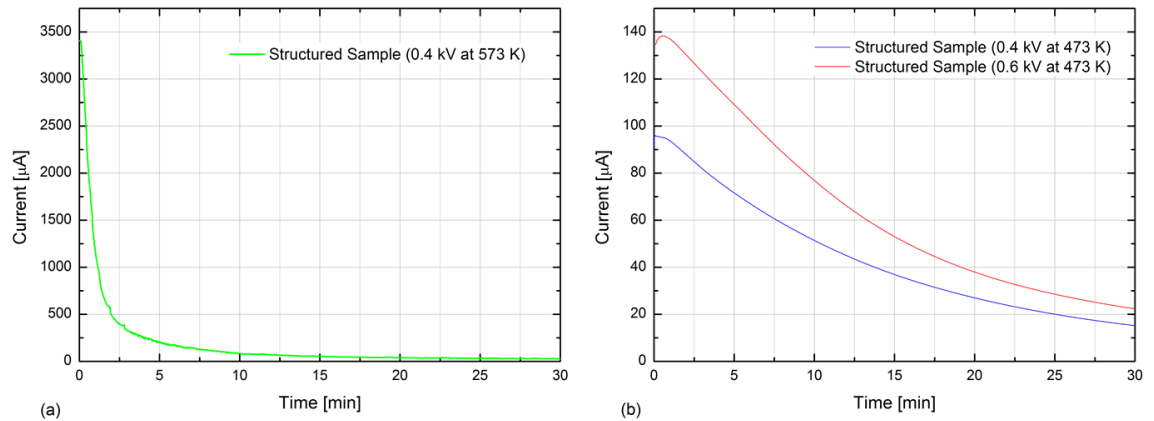
Fig. 35. The current-time dynamics of the samples structured at (a) (0.4 kV, 573 K), (b) (0.4 kV, 473 K) and (0.6 kV, 473 K).

The current-time dynamics in Fig. 35 (a) (b) are in stark contrast to that observed for the samples structured at (0.4 kV, 473 K) and (0.6 kV, 473 K) – Fig. 35 (b) . For instance, in the latter case (0.6 kV at 473 K), the current first rose to ~140 μA and then slowly decreased to below ~20 μA within 30 min with a resultant total charge transfer of ~0.08 A·s·cm^{-2}; this process resulted in the formation of the structures shown in Fig. 36 (b). Here the structures are just beneath the glass surface and the imprinted "scalloped" profile of the remaining "un-dissolved" nanoparticles is indicates a slow process which arises from the orthogonal electric field distribution.
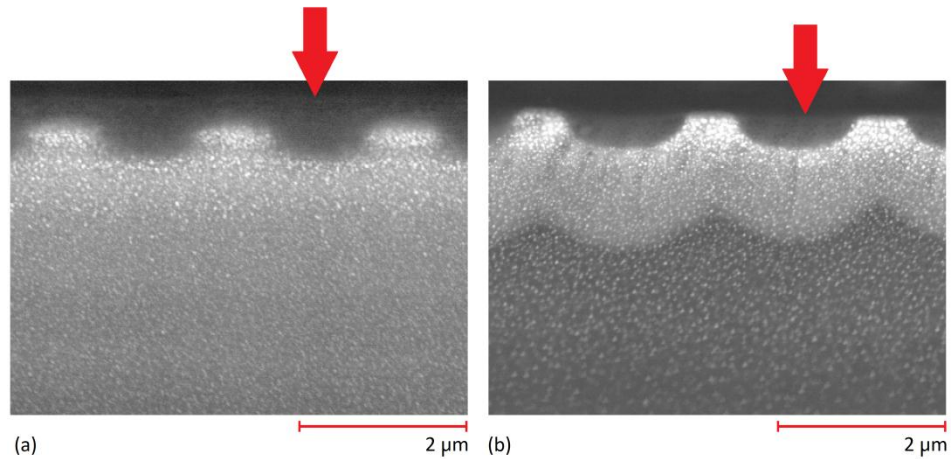
Fig. 36. SEM images of cross sections of samples modified at (a) (0.4 kV, 573 K) and (b) (0.6 kV, 473 K). Here the white colour is indicative of silver and black represents the dielectric matrix allowing the physical effect of structuring to be visible. Modification of the sample at (0.4 kV, 473 K) led to the formation of similar structures as seen in (b). Red arrows indicate surfaces.

Modification of the sample at (0.4 kV, 473 K) produced a total charge transfer of ~0.12 A·s·cm^{-2} and led to the formation of similar "scalloped" structures to those in Fig. 36 (b) indicating that this too was a slow structuring process.

It is worth pointing out that, looking back at Fig. 34, one could see that the amount of dissolved silver nanoparticles is the same for the samples structured at (0.4 kV, 573 K) - green line, and (0.6 kV, 473 K) – red line. In both cases, the SPR bands are narrowed down and blue shifted approximately by the same amount as compared to the original sample (Fig. 34 - black line). This is consistent with the very similar total charge transfer values for each of these processes. However, the results of the structuring (Fig. 36 (a) and (b)) are very different in terms of their size depth profile and shape.

From the graph presented in Fig. 35 (a) and the imprinted "castellated" shape of the cross-section in Fig. 36 (a) , one can conclude that in this case (0.4 kV, 573 K) a fast process initiated the observed space-selective dissolution process. As can be seen in Fig. 35 (b) reducing the temperature by 100 K results in a very different current-time dynamic behaviour.

The samples used for these experiments have a high filling factor of silver nanoparticles in the very near surface layer. Therefore, the potential barrier between two neighbouring metal clusters is low enough to make the thermally activated tunneling process possible [11]. This triggers the process and leads to the observed large current in Fig. 35. Further contribution to the process comes from the fact that at the applied temperature (573 K) more cations are available and contribute to the conduction mechanism. The cations in the glass, mainly Na^+, K^+, Ca^{2+}, become highly mobile (sodium in particularly) at elevated temperatures [54].

The applied dc electric field also leads to an ionic current flow and depletion of alkali and alkaline ions under the anode (beneath the nanoparticle-containing layer). This results in a space-charge region with a strong electric field falling across the nanoparticle-containing layer. The process leads to an electronic current from the nanoparticles towards anode where there is a contact with the structured anode. This makes the nanoparticles unstable and results in their selective dissolution in to glass matrix [10, 11, 57].

At the reduced temperature (473 K) - structuring processes presented in Fig. 35 (b) - the much lower current is due to the much-reduced mobility of the cations at this lower temperature. Here, the ionic nature of the observed current with no sign of a sudden rise due to electronic current is pronounced. This leads to a much slower dissolution process [57].

Fig. 37 represents a diffraction pattern of the structured sample whose cross-section was shown in Fig. 31 (b) . This is a typical "clean" diffraction pattern showing the ability of this technique to fabricate diffractive optical elements in glass with embedded metallic nanoparticles. The zero, first and second diffraction orders can easily be recognized. Similar diffraction patterns were observed from the samples structured at (0.4 kV, 473 K) and (0.4 kV, 573 K). Importantly for their application to optical elements, because the fabricated structures are beneath a thin glass layer, they are considered as robust and environmentally stable as the glass itself.
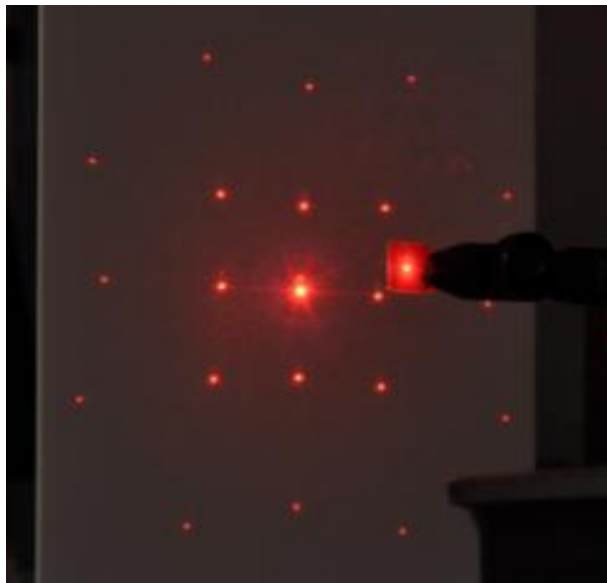
Fig. 37. Diffraction pattern (in transmission) of a sample of glass embedded with silver nanoparticles structured at (0.4 kV, 473 K, 30 min) upon He-Ne laser illumination. A similar diffraction pattern was observed from the sample structured at (0.6 kV, 473 K).

5.4. Summary

In summary, a diffractive optical element has been fabricated in a medium that has proven to be stable over centuries – glass containing metallic nanoparticles. The

fabrication technique was based on the dc electric field-assisted dissolution of the metallic nanoparticles in glass.

The experiments presented here offer the results for the most optimized structuring conditions: performing the experiment at higher voltages or temperatures leads to the full dissolution of the nanoparticles.

Chapter 6: Nanosecond puled laser interaction with glass embedded with silver nanoparticles

6.1. Introduction

Control of the size and shape of the metallic nanoparticles which are embedded in glass embedded with silver nanoparticles is crucial as this allows for the calculated modification of optical and structural properties of nanocomposites.

It has previously been shown that modification of embedded metallic nanoparticles can be achieved with the use of intense ultrashort laser pulses [67-69]. Femtosecond irradiation of glass embedded with silver nanoparticles has been shown to permanently modify the shape of the nanoparticle content; in particular it was discovered that spherical silver nanoparticles embedded in soda-lime float glass are permanently transformed into an ellipsoidal shape when irradiated with intense fs laser pulses at a wavelength near to the surface plasmon resonance [67-70]. Two methods of irradiation, multi-shot mode and single-shot regime, have been identified which result in different shapes. Multi-shot mode employs relatively low intensity pulses at a high rate on one spot resulting in the transformation of the initial nanospheres to prolate spheroids [70]. The single-shot regime uses higher intensity singular pulses which produce oblate spheroids [71]. The axis of symmetry of the embedded particles for both methods is orientated along the polarisation vector of the laser light. For both cases the modification of the nanoparticles is reversible by

heating the irradiated samples above the glass transition temperature (~873 K for

soda-lime float glass).

After fs irradiation there are significant changes to the SPR band position and

shape, Fig. 38. Post irradiation, for both methods, the SPR band splits into two

polarisation dependent bands. Multi-shot irradiation produces bands on different side

of the original SPR band; for polarisation parallel to that of the laser (p-polarised),

the peak position is shifted to longer wavelengths (red-shift), while for perpendicular

polarisation (s-polarised) the band is observed at a shorter wavelength (blue-shift).

This can be explained on the nanoscale by prolate silver spheroids with their

symmetry axes orientated along the direction of the laser polarisation, inset Fig.

38(a).
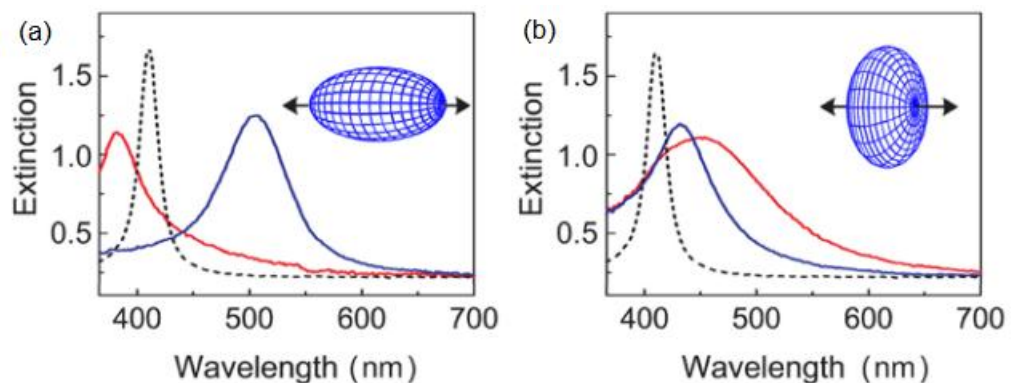
Fig. 38. Polarised extinction spectra of samples before and after fs

irradiation; (a) multi-shot mode (1000 pulses per spot, peak pulse intensity

$I_p = 0.6$ TW/cm^2), (b) single-shot regime ($I_p = 3$ TW/cm^2). The red line and

solid black likes respectively indicate s- and p-polarisation of the extinction

spectra.

For the single-shot regime the s-polarised band has a larger red shift than that

of the p-polarised band. Additionally both bands are shifted in this case. These

spectra are due to oblate Ag particles, inset Fig. 38 (b), again with their symmetry

axes orientated along the laser polarisation (horizontal).

However, there are no reports on the interaction of nanosecond laser pulses

with glass embedded with metallic nanoparticles. In this chapter, we will investigate

the optical and structural changes induced in silver-doped nanocomposite glass after

nanosecond pulsed laser irradiation. We also examine the effect, dependency and

importance of the number of pulses per spot fired into the nanocomposite, on the

laser's ability to manipulate the size and spatial distribution of the nanoparticles in a

single step.

6.2.   Experimental

Samples of silver-doped glass (produced using the method described on

pages 39-40) were irradiated using a Nd:YVO$_4$ laser, at $\lambda = 532$ nm and pulse length

of $\tau = 36$ ns, in standard atmospheric environment (room temperature and normal

pressure). The laser beam had a Gaussian intensity profile (M^2 < 1.3) and was

focused onto the target surface using a flat-field scanning lens system. The diameter

of the focused spot, between the points where the intensity had fallen to $1/e^2$ of the

central value, was $\phi \approx 60$ µm. This resulted in a Rayleigh range of ~ 4.8 mm, greater

than four times the thickness of the sample, leading to a negligible change of the

beam spot size on the target and providing a uniform beam trace throughout the

experiments. The important parameters of the laser used are summarised in Table 2.

Table 2. The details of the laser systems used which are significant to this work.

Laser system	GREEN-LASE 10W
Wavelength	532nm
Max mean output power	10 W± 5%
Emission type	Q-Switched
Max Pulse energy	350 μJ at 20kHz
Min Pulse duration	12 ns
Working frequency range	20kHz ~ 100kHz
Beam diameter, D_3	3.5 mm (at 4× beam expander output)
Beam divergence on the lens, θ_2	0.7 mrad
Focal of lens	160 mm
Real divergence after lens, θ_3	19.6 mrad
Nominal diameter of the focal spot, $2W_0$ (~ $2\omega_0$)	60 μm

A hatch distance of 60 μm was used in order to match the diameter of the beam. The repetition rate was kept constant, at f = 50 kHz, allowing for all experiments to be carried out using an average laser energy fluence of ~ 1.5 J/cm^2.
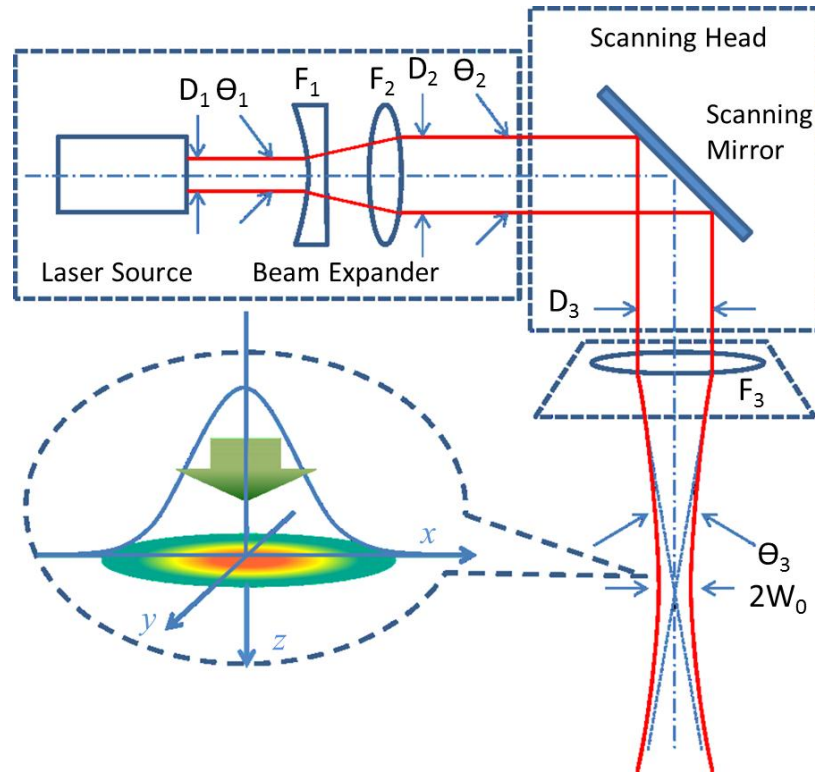
Fig. 39. An illustration of the optical path of the Nd:YVO$_4$ laser. D_1, D_2 and D_3 are the beam diameter at critical points; Θ_1, Θ_2 and Θ_3 indicate the beam divergences; F_1 and F_2 make up the beam expander; F_3 is an F-theta lens and finally W_0 shows the waist of the output beam. This figure has been adapted from [72].

The sample was characterised using a JASCO V-670 UV/VIS/NIR spectrophotometer, KEYENCE Digital Microscope VHX-1000, and a Hitachi S-4700 field emission scanning electron microscope (SEM).

6.3.   Results and Discussions

Six areas, all 16 mm^2 in size, were irradiated at six different scanning speeds, Fig. 40. By selecting the appropriate scanning speeds, it was possible to vary the number of pulses being fired per spot, N, from 100 to 600 (in steps of 100 pulses per spot).
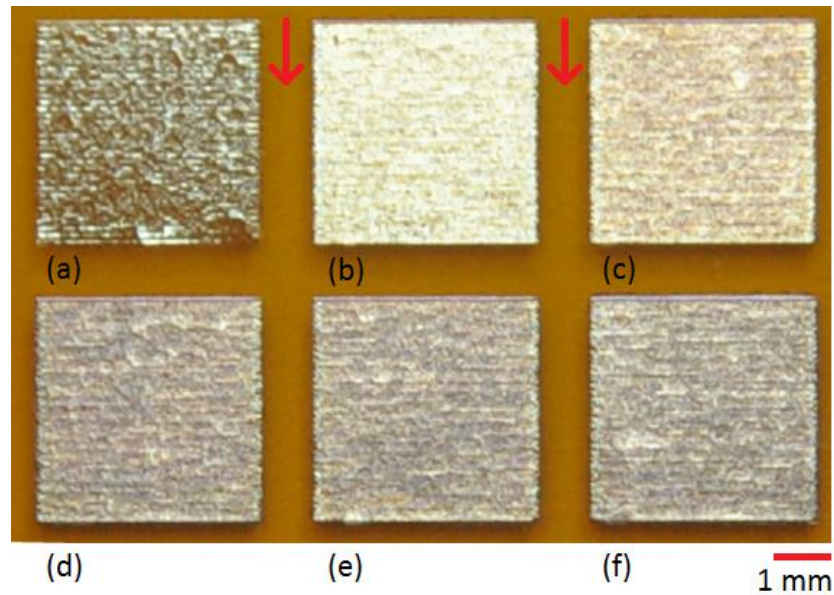
Fig. 40. Photograph of all six exposed areas, which were irradiated at (a) 100, (b) 200, (c) 300, (d) 400, (e) 500 and (f) 600 pulses per spot. In these images the silver film at the surface can be clearly seen against the background of silver nanoparticle embedded glass, which appears yellow in colour (indicated by the red arrows).

The conductivity of the glass before and after irradiation was measured in order to gain a better understating of how the irradiation affects the structure of the glass; the results of which can be seen in Fig. 41. (Please refer to chapter 3 for a detailed description of how the conductivity of such samples is measured and presented.)
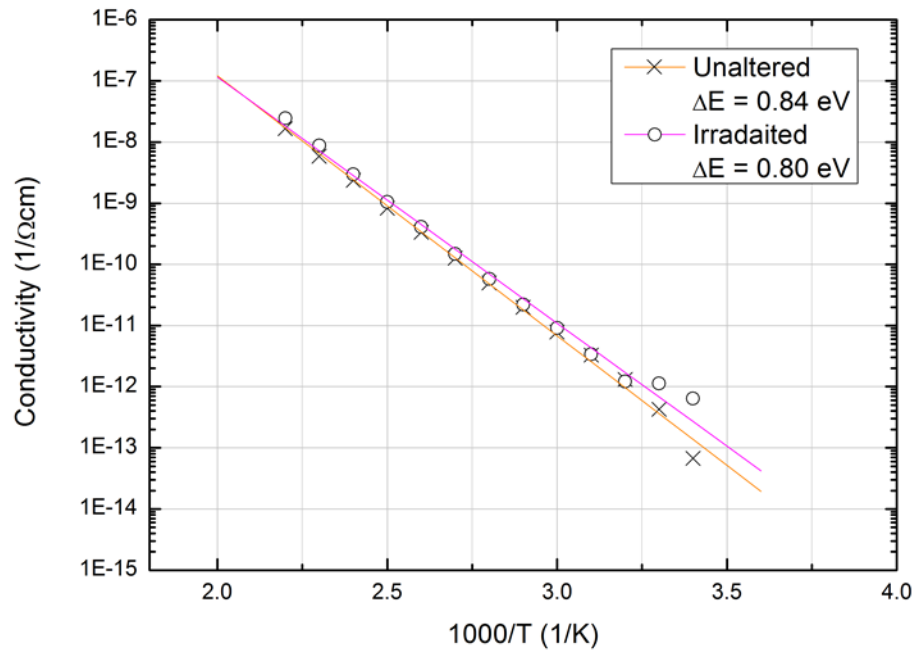
Fig. 41. Conductivity measurements for a sample of glass embedded with silver nanoparticles before ("Unaltered") and after ("Irradiated") irradiation at a constant fluence of ~ 1.5 J/cm^2 with 300 pulses per spot. For the conductivity measurements a larger irradiated area was required in order to accommodate the gap cells (Fig. 20)Fig. 18. Photographs showing deposited gold electrodes on (a) a sample of unaltered soda-lime float glass and (b) an unaltered sample of glass embedded with silver nanoparticles. Due to some slight damage (visible in photographs) these were not the electrodes used for the measurements; however electrodes deposited in the same manner were used and these images serve to show how these appeared on the glass samples. and so an exposed area of 1.76 cm^2 was produced at 300 pulses per spot (chosen as this was mid-range of the number of pulses being investigated). The key shows the activation energy of both samples.

The results indicated that post irradiation the conductivity of the glass had increased this would suggest either an increase in the concentration *or* the mobility of charge

carriers in the glass after exposure. The activation energy of the irradiated area had

decreased to 0.80 eV (from 0.84 eV for the unaltered sample).
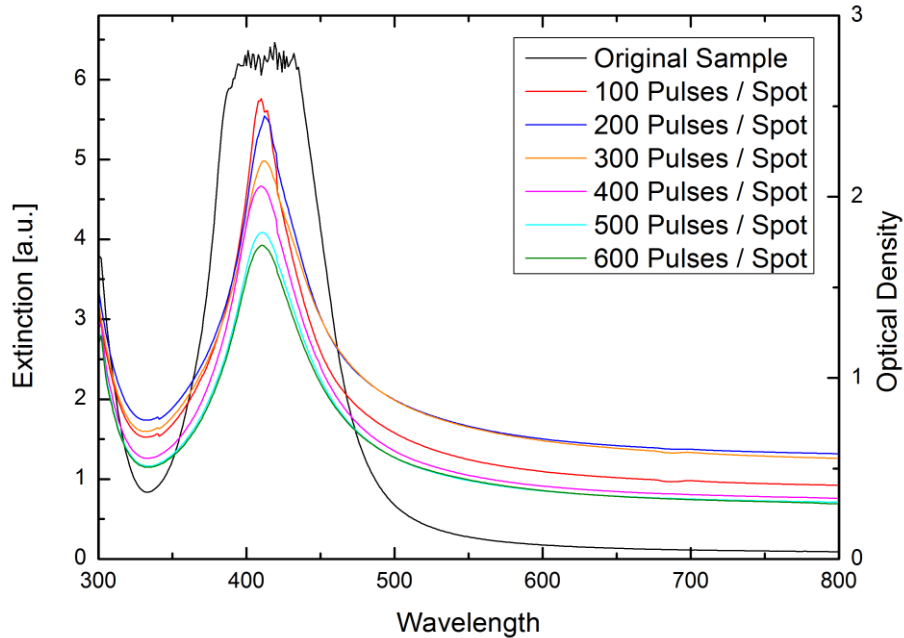
Fig. 42. Measured extinction spectra of glass embedded with silver
nanoparticles before irradiation (black line) and the six areas after
irradiation, at a constant fluence of ~ 1.5 J/cm^2, with varying number of
pulses from 100 to 600 pulses per spot (indicated in the key).

Extinction spectra were taken on six irradiated areas and compared with the

original pre-irradiated sample in Fig. 42. of all six irradiated areas were taken and

compared to the original sample area. The extinction spectrum for the original

sample (black line) is clearly saturated, indicating very strong absorption relative to

the subsequent spectra taken after laser irradiation. These peaks are progressively

reduced in height with increasing number of laser pulses per spot. However there is

no evidence for a corresponding reduction in peak width. Maxwell-Garnett theory

predicts a reduction in both peak height and width if the average radius of silver

inclusions in the glass matrix increases and the volume filling factor decreases [8,

28, 71]. It can also be seen that, with increasing the number of pulses per spot there is a noticeable decrease in the peak of the SPR band. This is seen in Fig. 10 (b) and indicates that with increasing number of pulses per spot the volume filling factor of metal inclusions decreases.

The spectra also show an increase in the optical density at longer wavelengths. This is due to the formation and subsequent increase of the thickness of the produced surface films after irradiation [73]. This surface film can clearly be seen in the images of the irradiated areas after irradiation (Fig. 40).

The particle size of the silver inclusions for each irradiated area was investigated with the use of SEM imaging; Fig. 43.
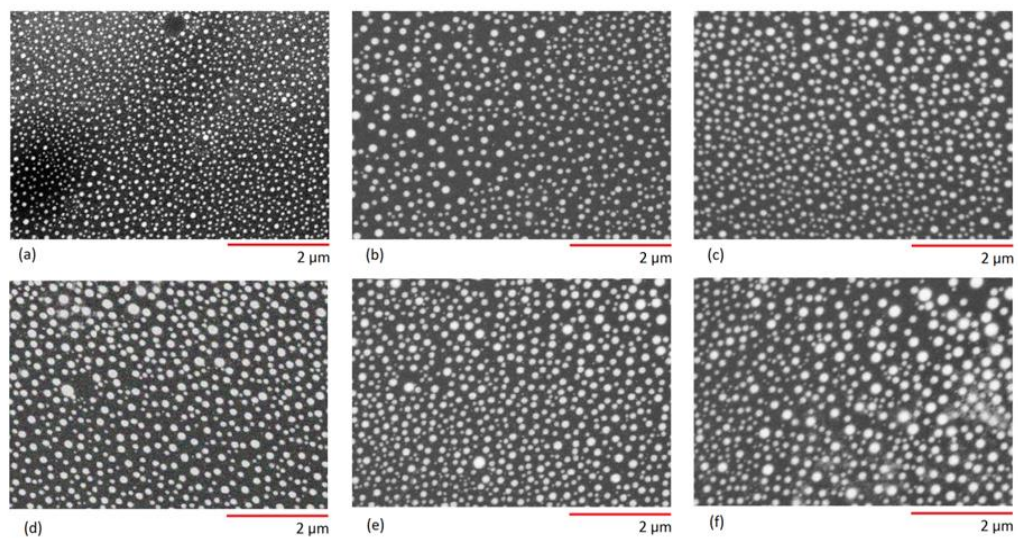
Fig. 43. SEM images of glass embedded with silver nanoparticles after irradiation at (a) 100, (b) 200, (c) 300, (d) 400, (e) 500 and (f) 600 pulses per spot.

The average particle sizes in each of the six irradiated areas were then measured from the images taken and the results were plotted; Fig. 44.
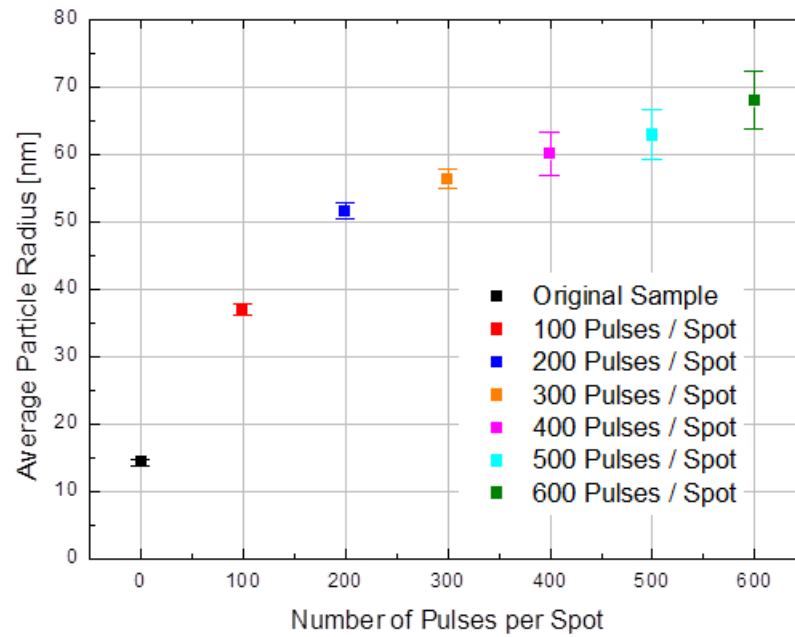
Fig. 44. Plot displaying the average particle size before and after irradiation. Post irradiation the particle size has increased and continues to do so with increasing number of pulses per spot.

From this plot it is clearly visible that irradiation of glass embedded with silver nanoparticles results in an increase in the average particle size. It is also evident that a greater number of pulses per spot further increased the particle size.

A rough estimate of the approximate values of temperature reached during the irradiation will provide an insight into the process. The change in temperature, as a result of irradiation, was calculated in terms of the optical properties of the glass used. As can be seen in Fig. 8 (b), the concentration of silver nanoparticles, and hence the absorption coefficient, α, varies with depth, z. This variation in the absorption coefficient can be described in terms of an exponential function;

$$\alpha(z) = \alpha_0 \exp\left(\frac{-2z}{l}\right),$$
25

where α_0 is the absorption coefficient at the glass surface (i.e. the maximum absorption coefficient) and l is the thickness of the nanoparticle containing layer. Using this equation and the Beer-Lambert law, the following expression can be obtained for the change in transmittance, T, with depth;

$$T(z) = \frac{I(z)}{I_0} = \exp\left[\frac{\alpha_0 l}{2}\left[\exp\left(\frac{-2z}{l}\right) - 1\right]\right] \qquad 26$$

where I_0 and $I(z)$ are the intensity of the incident light and the intensity as it varies with depth, respectively. This expression clearly shows that if the depth is much greater than the thickness of the nanoparticle containing layer (i.e. $z \gg l$), which is true as $\alpha(z) \rightarrow 0$, then $T(z)$ reduces to a constant, which is the total transmittance, T;

$$T(z) \rightarrow T = \exp\left(\frac{-\alpha_0 l}{2}\right) \qquad 27$$

Using the spectrophotometer, the transmittance, T_m, and reflectivity, R_m, of the glass used was measured. The relationship between the measured transmittance and the total transmittance is as follows;

$$T_m = (1 - R_{Ag})(1 - R_G)T \qquad 28$$

where R_{Ag} is the pure reflectance at the silver containing layer surface and R_G is the reflectivity at the glass-air interface, and is measured to be 4%. The relationship between these values and the measured reflectance is given by;

$$R_m \approx R_{Ag} + R_G(1 - R_{Ag})^2 T^2 \qquad 29$$

Using the measured values, and their corresponding equations, it is therefore possible to calculate the maximum absorption coefficient by rearranging Eq. 27;

$$\alpha_0 = -\frac{2}{l}\ln(T) = \frac{2}{l}\left[\ln(1 - R_{Ag}) + \ln(1 - R_G) - \ln(T_m)\right] \qquad 30$$

Going back to the Beer-Lambert law, the change in intensity for a varying absorption

coefficient is defined as;

$$dI(z) = -\alpha(z)I_0 dz \qquad\qquad 31$$

Solving this equation and substituting for $\alpha(z)$ (Eq. 25), the intensity, as it varies with

depth, can be expressed as;

$$I(z) = T(z)I_0 = I_0 \exp\left[\frac{\alpha_0 l}{2}\left[\exp\left(\frac{-2z}{l}\right) - 1\right]\right] \qquad\qquad 32$$

This gives the intensity with depth only. On the surface of the glass (i.e. the (x,y)

plane) the intensity $(I(x,y,t))$ is governed by a Gaussian distribution and so the

intensity on the glass surface (with time) can be defined as;

$$I(x,y,z,t) = I_0(t)\exp\left(\frac{-2x^2}{\omega_0^2} - \frac{-2y^2}{\omega_0^2}\right)T(z) \qquad\qquad 33$$

where ω_0 is the beam radius. If we assume that the incident heat is kept in the same

position, then the change in temperature distribution, ΔT (not to be confused with

transmittance, T), can be calculated in terms of the change in the absorption

coefficient with depth and the variation in intensity with (x,y,z). The change in

temperature distribution, ΔT, after one pulse, may therefore be expressed as [74];

$$\Delta T(x,y,z) = \frac{\alpha(z)}{\rho C_p}\int I(x,y,z,t)dt = \frac{\alpha(z)}{\rho C_p}F(x,y)T(z) \qquad\qquad 34$$

where ρ is the density, taken as 2.47 g/cm^3 [75] (this value, taken from the literature,

is for silver ion exchange glass but should provide a reasonable estimate for surface

temperature in our case) and Cp is the specific heat capacity taken as 0.84 J/gK (the

value for glass) [75]. The surface fluence, $F(x,y)$, is governed by a Gaussian

distribution and thus may be defined as following:

$$F(x, y) = F_0 \exp\left(\frac{-2x^2}{\omega_0^2} - \frac{2y^2}{\omega_0^2} \right)$$ 35

Substituting for $a(z)$ (Eq. 25) and $I(x,y,z)$ (Eqs. 26 and 33) gives;

$$\Delta T(x, y, z) = \frac{\alpha_0 \exp\left(-2z/l \right)}{\rho C_p}(1 - R_{Ag})F(x, y)\exp\left[\frac{\alpha_0 l}{2}\left[\exp\left(\frac{-2z}{l} \right) - 1 \right] \right]$$ 36

Here, the (1-R_{Ag}) term is to compensate for energy that is lost due to reflection at the silver nanoparticle containing layer surface. The greatest increase in temperature will occur at the origin ($\Delta T(0,0,0)$), therefore from Eq. 36 the maximum resultant temperature change after one pulse is ~873 K. This rise in temperature is above the glass softening temperature for the glass used in these experiments which is around 800 K. This assessment is reasonable since we observed some melting of the glass surface in our experiments. In fact for pulse durations (typically > 0.1 ns), exceeding the time for heating of the medium, the heat is being absorbed and delivered in the surroundings simultaneously. In these cases, typically occurring during nanosecond pulse laser irradiation of nanoparticles, the heating duration simply equals the pulse duration [76]. This, in combination with the fact that pulsed (as compared to continuous wave) irradiation in the vicinity of the SPR band makes it possible to further confine the temperature increase to the vicinity of the nanoparticles, justifies the temperature estimate here to be considered as a model for the laser heating and melting.

Hence, it is plausible that irradiation results in the glass, and therefore the silver embedded within it, to be in a molten phase. As two immiscible liquids the glass and silver then undergo coalescence with creaming, leading to the well-known phenomenon of Ostwald ripening [77]. At irradiances well above the melt threshold

uniform melting occurs. This results in the excitation of convective fluxes within the liquid layer due to lateral variations of the melt temperature. The surface tension of melt decreases with temperature, and liquid tends to be pulled away from hotter towards cooler regions, with silver drawn out to the edges of the melt meniscus. Therefore the formation of a thin film of silver particles is observed. This migration also increases the probability of coalescence and Ostwald ripening as it decreases the separation distance between the silver particles. In order to better understand the results seen here additional experiments are required to show effects of varying other parameters besides the number of pulses per spot (such as volume filling factor). More advanced modelling, perhaps building on the work presented in [78, 79], is also needed to show precisely how the temperature difference changes with number of pulses per spot.

6.4.   Summary

The modification of glass with embedded silver nanoparticles upon nanosecond (36 ns) pulsed Nd:YVO$_4$ laser irradiation at 532 nm was demonstrated. Using a laser energy fluence of ~ 1.5 J/cm^2 it was possible to form a silver nanoparticle containing film on the surface of the glass. Increasing the applied number of pulses to the sample resulted in the increase of the average size of the nanoparticles from 15 nm to 35 − 80 nm in radius. It was shown that the increase in size is a result of the thermal interaction of the pulses and therefore a higher number of pulses per spot produced a greater increase in particle size. Irradiation of the glass composite promoted the formation of a surface film of larger nanoparticles.

The controlled modification of the nanoparticles described in this process allows for the tuning of optical and structural properties of metal-glass

nanocomposites, making this process suitable for the production of complex optical elements and for aesthetic applications an example of which is shown in Fig. 45 - where by varying the number of pulses per spot different 'shades' were produced to form a visual effect.

Fig. 45. (a) and (b) Two samples of glass embedded with silver nanoparticles which have been irradiated for the purpose of visual effect. The different 'shades' are produced by varying the laser energy fluence which creates these aesthetically pleasing designs.

A thermal model was used to estimate the temperature rise due to the irradiation process and showed that the change in temperature was above that of the glass softening temperature. This suggests that during irradiation the glass, and silver nanoparticles embedded within in it are in a molten phase. This controlled localized melting and reforming of the silver nanoparticles is a fundamentally different process to the size and shape modification of metallic nanoparticles by ultrashort laser pulses with the longer timeframe enabling an emulsive interaction between the molten phases of the nanoparticle and host matrix.

The simplicity and flexibility of the nanosecond pulsed laser irradiation technique allows for the creation of complex, reproducible patterns of larger nanoparticles with smaller separation distances within glass embedded with silver nanoparticles. This allows for tuning the optical and structural properties of the nanocomposite. These can then serve as substrates for sensing and surface enhanced Raman spectroscopy (SERS) applications.

Chapter 7: Conclusions and Future Outlook

The modification of glass and glass embedded with silver nanoparticles has been carried out in a number of different ways. These materials have optical and aesthetic applications, with wider implications across the field of physics and beyond.

The first process, thermal poling of 'pure' soda-lime float glass demonstrated the modification of the glass structure by re-distribution of positive ions, which was analysed using X-ray element analysis.

A variation of the thermal poling process, EFAD, was then applied to glass embedded with silver nanoparticles. This resulted not in a restructuring of the glass itself but rather in a dissolution of the silver nanoparticles within the glass matrix; an effect visible to the naked eye as the area of glass which had been in contact with the electrode became more transparent and of a lighter colouring than the original sample area post process. This difference in volume fill factor of the processed glass compared to that of the unaltered silver-embedded glass was shown to be in agreement with the signs of reduced volume fill factor using Maxwell-Garnett theory.

To further analyse the effect poling has on both the pure glass and the glass embedded with silver nanoparticles the conductivity of the glasses was measured before and after poling. The results showed that post-poling both types of glasses had a significant decrease in conductivity owing to the decrease in available positive charge carriers (sodium and potassium for the pure glass and silver for the metal embedded glass).

The thermal poling procedure was then developed by utilising more complex methods of poling; this was achieved by introducing patterned electrodes. Samples of "pure" soda-lime float glass were poled this way enabling effective diffraction gratings with varying degrees of diffraction efficiency to be fabricated, allowing for the establishment of optimal structuring conditions.

By comparison of the conductivity measurements of the grid structured sample of pure glass to those of the unaltered and the plain poled samples it was shown that as with the plain electrode poling the fabrication method results in the re-structuring of the glass itself and therefore causes a variation in the refractive index. However in this instance the presence of the structured electrode allows for the selective re-structuring of the glass and hence the refractive index varied periodically throughout the modified sample and was responsible for the diffraction pattern produced. As this process alters the structure of the glass itself and is not a coating or etching of the surface the process makes for much more robust and resilient diffractive optical elements.

The effectiveness of the diffraction gratings was then assessed by calculating the diffraction efficiencies of the fabricated samples. The results showed that the sample modified at a maximum voltage of 0.3 kV produced the most effective DOE and it was therefore these parameters that were used in order to produce a more complex pattern by repeating the poling process at a different angle. This demonstrated that the diffraction pattern itself is governed completely by the electrode used and so by altering the pattern of the electrode more complex diffraction patterns could be achieved and replicated.

EFAD of glass embedded with silver nanoparticles was also successfully performed using the patterned electrodes. The experiments presented offered the

results for the most optimized structuring conditions: performing the experiment at higher voltage or temperature led to more complete dissolution of the nanoparticles. As glass embedded with silver nanoparticles is such a resilient glass known to be stable over many centuries, meaning these diffraction gratings are not only effective but also more robust and cost effective in comparison to the rival gratings in use.

The modification of glass with embedded silver nanoparticles upon nanosecond (36 ns) pulsed Nd:YVO$_4$ laser irradiation at 532 nm was the last to be demonstrated. Using a laser energy fluence of ~1.5 J/cm^2 created a silver nanoparticle containing film on the surface of the glass. Increasing the applied number of pulses to the sample increased both the average size of the nanoparticles, from 15 nm to $35 - 80$ nm in radius, and the thickness of the surface film.

By employing a thermal model the temperature rise due to the irradiation process was estimated and showed that the change in temperature of the glass under irradiation was well above that of the glass softening temperature. This indicates that during nanosecond irradiation of glass embedded with silver nanoparticles the glass, and therefore the silver embedded within, are in a molten phase.

This nanosecond pulsed laser irradiation technique while very simple allows for the creation of complex, reproducible patterns of larger nanoparticles with smaller separation distances within glass embedded with silver nanoparticles, with the limiting factor on the pattern produced being the program used to control the laser. This allows for precise modification of the nanoparticles and therefore offers detailed tuning of the optical and structural properties of the nanocomposite material. With these options available glass embedded with silver nanoparticles may be adapted to serve as substrates for sensing and surface enhanced Raman spectroscopy (SERS) applications.

In the future the applications of this work may be realised from the field of optics to the creative industry. More robust diffractive optical elements are needed as the diffraction gratings currently available are both fragile and expensive; it is therefore desirable to have a cost effective, viable alternative. Laser irradiation of glass embedded with silver nanoparticles has a great deal of potential not only because of the unique visual effects that may be produced but also because the fine tuning of the optical and structural properties of the nanocomposite make it a promising material as they can serve as substrates for sensing and SERS applications.

References

1. R. A. Myers, N. Mukherjee, and S. R. J. Brueck, "Large second-order nonlinearity in poled fused silica," Opt. Lett. **16**(22), 1732–1734 (1991).

2. P. G. Kazansky, A. Kamal, and P. St. J. Russell, "High second-order nonlinearities induced in lead silicate glass by electron-beam irradiation," Opt. Lett. **18**(9), 693–695 (1993).

3. D. Faccio, V. Pruneri, and P. G. Kazansky, "Dynamics of the second-order nonlinearity in thermally poled silica glass," Appl. Phys. Lett. **79**(17), 2687–2689 (2001).

4. F. C. Garcia, I. C. S. Carvalho, E. Hering, W. Margulis, and B. Lesche, "Inducing a large second-order nonlinearity in soft glasses by poling," Appl. Phys. Lett. **72**(25), 3252–3254 (1998).

5. M. Dussauze, V. Rodriguez, A. Lipovskii, M. Petrov, C. Smith, K. Richardson, T. Cardinal, E. Fargin, and E. I. Kamitsos, "How does thermal poling affect the structure of soda-lime glass?" J. Phys. Chem. C **114**(29), 12754–12759 (2010).

6. N. Godbout and S. Lacroix, "Characterisation of thermal poling in silica glasses by current measurements," J. Non-Cryst, Solids **316**(2–3), 338–348 (2003).

7. K. L. Kelly, E. Coronado, L. L. Zhao, and G. C. Schatz, "The optical properties of metal nanoparticles: The influence of size, shape, and dielectric environment," J. Phys. Chem. B **107**(3), 668–677 (2003).

8. A. Podlipensky, A. Abdolvand, G. Seifert, and H. Graener, "Femtosecond laser assisted production of dichroitic 3D structures in composite glass containing Ag nanoparticles," Appl. Phys., A Mater. Sci. Process. **80**(8), 1647–1652 (2005).

9. A. Abdolvand, A. Podlipensky, S. Matthias, F. Syrowatka, U. Gösele, G. Seifert, and H. Graener, "Metallodielectric two-dimensional photonic structures made by electric field microstructuring of nanocomposite glass," Adv. Mater. (Deerfield Beach Fla.) **17**(24), 2983–2987 (2005).

10. O. Deparis, P. G. Kazansky, A. Abdolvand, A. Podlipensky, G. Seifert, and H. Graener, "Poling-assisted bleaching of metal-doped nanocomposite glass," Appl. Phys. Lett. **85**(6), 872–874 (2004).

11. A. Podlipensky, A. Abdolvand, G. Seifert, H. Graener, O. Deparis, and P. G. Kazansky, "Dissolution of silver nanoparticles in glass through an intense dc electric field," J. Phys. Chem. B **108**(46), 17699–17702 (2004).

12. U. Kreibig and M. Vollmer, *Optical Properties of Metal Clusters* Springer (1995).

13. M. L. Brongersma and P.G. Kik, *Surface Plasmon Nanophotonics*, Springer (2007).

14. L. Loomba, and T. Scarabelli, "Metallic nanoparticles and their medical potential. Part II: gold and silver colloids," Ther. Deliv. **4**(7), 859-873 (2013).

15. L. Loomba, and T. Scarabelli, "Metallic nanoparticles and their medical potential. Part II: aluminosilicates, nanobiomagnets, quantum dots and cochleates," Ther. Deliv. **4**(9), 1179-1196 (2013).

16. M. C. Edmundson, M. Capeness, and L. Horsfall, "Exploring the potential of metallic nanoparticles within synthetic biology," N. Biotechnol. **31**(6), 572-578 (2014).

17. K. N. Thakkar, S. S. Mhatre, and R. Y. Parikh, "Biological sysnthesis of metallic nanoparticles," Nanomed. Nananotech. Biol. Med. **6**(2), 257-262 (2010).

18. M-C. Daniel and D. Astruc, "Gold nanoparticles: assembly, supramolecular chemistry, quantum-size-related properties, and applications toward biology, catalysis, and nanotechnology," Chem. Rev. **104**(1), 293-346 (2004).

19. W. J. Wing, S. M. Sadeghi, R. R. Gutha, Q. Campbell, and C. Mao, "Metallic nanoparticle shape and size effects on aluminum oxide-induced enhancement of exciton-plasmon coupling and quantum dot emission," J. Appl. Phys. **118**, 124302 (2015).

20. K. An and G. A. Samorjai, "Size and Shape Control of Metal Nanoparticles for Reaction Selectivity in Catalysis," ChemCatChem **4**(10), 1512-1524 (2012).

21. J. M. Campelo, D. Luna, R. Luque, J. M. Marinas, and A. A. Romero, "Sustainable preparation of supported metal nanoparticles and their applications in catalysis," ChemSusChem. **2**(1), 18-45 (2009).

22. R. J. White, R. Luque, V. L. Budarin, J. H. Clark, and D. J. Macguarrie, "Supported metal nanoparticles on porous materials. Methods and applications," Chem. Soc. Rev. **38**, 481-494 (2009).

23. J.-T. Lue, "A review of characterization and physical property studies of metallic nanoparticles," J. Phys. Chem. Solids **62**(9-10), 1599-1612 (2001).

24. J.-Y. Bigot, V. Halté, J.-C. Merle, and A. Daunois, "Electron dynamics in metallic nanoparticles," Chem. Phys. **251**(1-3), 181-203 (2000).

25. Y. Cheng, M. Masuda, K. Shihoyama, K. Toyoda, and K. Midorikawa, "Optical gratings embedded in photosensitive glass by photochemical reaction using a femtosecond laser," Opt. Express **11**(15), 1809-1816 (2003).

26. T. Som and B. Karmakar, "Surface plasmon resonance and enhanced fluorescence application of single-step synthesized elliptical nano gold-embedded antimony glass dichroic nanocomposites," Plasmonics **5**(2), 149-159 (2010).

27. R. D. Guenther, *Modern Optics* (1990, Wiley).

28. V. M. Shalaev, *Optical Properties of Nanostructured Random Media,* Springer (2001).

29.   A. Stalmashonak (2009), *Laser-induced shape transformation of silver nanoparticles embedded in glass.* Unpublished PhD thesis. Martin Luther University of Halle-Wittenberg.

30.   R. Jin, Y. Charles Cao, E. Hao, G. S. Métraux, G. C. Schatz, and C. A. Mirkin, "Controlling anisotropic nanoparticle growth through plasmon excitation," Nature **425**(6957), 487–490 (2003).

31.   M. S. Gudiksen, L. J. Lauhon, J. Wang, D. C. Smith, and C. M. Lieber, "Growth of nanowire superlattice structures for nanoscale photonics and electronics," Nature **415**(6872), 617–620 (2002).

32.   S. Verma, B. T. Rao, S. Rai, V. Ganesan, and L. M. Kukreja, "Influence of process parameters on surface plasmon resonance characteristics of densely packed gold nanoparticle films grown by pulsed laser deposition," Appl. Surf. Sci. **258**(11), 4898-4905 (2012).

33.   G. Mie, "Beiträge zur optik trüber medien, speziell kolloidaler metallösungen," Ann. Phys. **330**(3), 377-445 (1908).

34.   C. F. Bohren and D. R. Huffman, *Absorption and scattering of light by small particles* (Wiley, 1983).

35.   V. V. Kresin, "Collective resonances in silver clusters: Role of d electrons and the polarization-free surface layer," Phys. Rev. B **51**(3), 1844-1899 (1995).

36.   K.-J. Berg, A. Berger, and H. Hofmeister, "Small silver particles in glass layers produced by sodium-silver ion exchange – their concentration and size depth profile," Z. Phys. D **20**(1) 309-311 (1991).

37.   A. Hilger, M. Tenfelde, and U. Kreibig, "Silver nanoparticles deposited on dielectric surfaces," Appl. Phys. B **73**(4), 361-372 (2001).

38.   S. Link and M. A. El-Sayed, "Optical properties and ultrafast dynamics of metallic

nanocrystals," Ann. Rev. Phys. Chem. **53**, 331-366 (2003).

39. S. Berciaud, L. Cognet, P. Tamarat, and B Lounis, "Observation of intrinsic size effects in the optical response of individual gold nanoparticles," Nano. Lett. **5**(3), 515-519 (2005).

40. M. P. Seah and W. A. Dench, "Quantitative electron spectroscopy of surfaces: A standard data base for electron inelastic mean free paths in solids," Surf. Interface. Anal. **1**(1), 2-11 (1979).

41. U. Kreibig and L. Genzel, "Optical absorption of small metallic particles," Surf. Sci. **156**(2), 678-700 (1985).

42. V. Amendola and M. Meneghetti, "Size Evaluation of Gold Nanoparticles by UV−vis Spectroscopy," J. Phys. Chem. C **113**(11), 4277-4285 (2009).

43. J. C. M. Garnett, "Colours in metal glasses in metallic films, and in metallic solutions. II," Philos. Trans. R. Soc. A **203**, 385-420 (1905).

44. J. P. Martin and J. R. Lemon, "Optical properties of aggregated metal systems. I. Theory," Phys. Rev. B. **4**, 271 (1971).

45. V. A. Markel, V. Shalaev, E. B. Stechel, W. Kim, R. L. Armstrong, "Small-particle composites. I. Linear optical properties," Phys. Rev. B **53**, 2425 (1998).

46. S. V. Karpov, A. L. Basko, A. K. Popov, V. V. Slabko, T. F. George, "Optics of Nanostructured Fractal Silver Colloids," Chapter in *Resent Research Developments in Optics, Vol. 2* pp. 427-463 (Research Signpost, 2002).

47. B. Lamprecht, A. Leitner, and F. G. Ausseneg, "Femtosecond decay-time measurement of electron-plasma oscillation in nanolithographically designed silver particles," Appl. Phys. B **64**(2), 269-272 (1997).

48. G. Xu, M. Tazawa, P. Jin, and S. Nakao, "Surface plasmon resonance of sputtered Ag films: substrate and mass thickness dependence," Appl. Phys. A **80**, 1535-1540

(2005).

49.   M. Qui, T. Mizunami, R. Vilaseca, F. Pi, and G. Orriols, "Bulk and near-surface second-order nonlinearities generated in a BK7 soft glass by thermal poling," J. Opt. Soc. Am. B **19**(1), 37–42 (2002).

50.   A. L. C. Triques, C. M. B. Cordeiro, V. Balestrieri, B. Lesche, W. Margulis, and I. C. S. Carvalho, "Depletion region in thermally poled fused silica," Appl. Phys. Lett. **76**(18), 2496–2498 (2000).

51.   A. A. Lipovskii, V. G. Melehin, M. I. Petrov, Yu. P. Svirko, and V. V. Zhurikhina, "Bleaching versus poling: Comparison of electric field induced phenomena in glasses and glass-metal nanocomposites," J. Appl. Phys. **109**(1), 011101 (2011).

52.   Y. Fujii, B. Kawasaky, K. O. Hill, and D. C. Johnson, "Sum-frequency light generation in optical fibers," Opt. Lett. **5**(2), 48-50 (1980).

53.   U. Osterberg and W. Margulis, "Dye laser pumped by Nd:YAG laser pulses frequency doubled in a glass optical fiber," Opt. Lett. **11**(8), 516-518 (1986).

54.   P. G. Kazansky and P.St.J. Russel, "Thermally poled glass: frozen-in electric field or oriented dipoles?" Opt. Commun. **110**, 611-614 (1994).

55.   A. L. R. Brennand and J. S. Wilkinson, "Planar waveguides in multicomponent glasses fabricated by field-driven differential drift of cations," Opt. Lett. **27**(11), 906–908 (2002).

56.   A. A. Lipovskii, V. G. Melehin, M. I. Petrov, Yu. P. Svirko, and V. V. Zhurikhina, "Bleaching versus poling: Comparison of electric field induced phenomena in glasses and glass-metal nanocomposites," J. Appl. Phys. **109**(1), 011101 (2011).

57.   A. Abdolvand, A. Podlipensky, G. Seifert, H. Graener, O. Deparis and P. G. Kazansky, "Electric field assisted formation of percolated silver nanolayers inside glass," Opt. Exp. **13**, 1266-1274 (2005).

58. J. Sancho-Parramon, A. Abdolvand, A. Podlipensky, G. Seifert and H. Graener, "Modeling of optical properties of silver-doped nanocomposite glasses modified by electric-field-assisted dissolution of nanoparticles," Appl. Opt. **45**, 8874-8881 (2006).

59. R. H. Doremus, "Mechanism of electrical polarization of silica glass," Appl. Phys. Lett. **87**(23), 232904 (2005).

60. K. Sokolv, V. Melehin, M. Petrov, V. Zhurikhina, and A. Lipovskii, "Spatially periodical poling of silica glass," J. Appl. Phys. **111**(10), 104307 (2012).

61. V. Lehmann, "The Physics of Macropore Formation in Low Doped n-Type Silicon," J. Electrochem. Soc. **140**, 2836 (1993).

62. MPI: Ordered Porous Materials. http://www-old.mpi-halle.mpg.de/department2/research-areas/ordered-porous-materials/ (accessed February 2016).

63. T. Rogers and J. Kowal, "Selection of glass, anodic bonding conditions and material compatibility for silicon-glass capacitive sensor," Sens. Actuators, A **46**(1-3), 113-120 (1995).

64. M. Despont, H. Gross, F. Arrouy, C. Stebler, U. Staufer, "Fabrication of a silicon-Pyrex-silicon stack by a.c. anodic bonding," Sens. Actuators, A **55**(2-3), 219-224 (1996).

65. O. Deparis, P. G. Kazansky, A. Podlipensky, A. Abdolvand, G. Seifert, and H. Graener, "Evolution of poling assisted bleaching of metal-doped nanocomposite glass with poling conditions," App. Phys. Lett. **86**, 261109 (2005).

66. A. Stalmashonak, G. Seifert, A. A. Unal, U. Skrzypczak, A. Podlipensky, A. Abdolvand, and H. Graener, "Toward the production of micropolarizers by irradiation of composite glasses with silver nanoparticles," Appl. Opt. **48**(25), F37-

F43 (2009).

67. M. Kaempfe, T. Rainer K.-J. Berg, G. Seifert, H. Graener. "Ultrashort laser pulse induced deformation of silver nanoparticles in glass," Appl. Phys. Lett. **74**, 1200 (1999).

68. M. Kaempfe, G. Seifert, K.-J. Berg, H. Hofmeister H. Graener. "Polarization dependence of the permanent deformation of silver nanoparticles in glass by ultrashort laser pulses," Eur. Phys. J. D **16**(1), 237-240 (2001).

69. G. Seifert, M. Kaempfe, K.-J. Berg, H. Graener. "Production of "dichroitic" diffraction gratings in glasses containing silver nanoparticles via particle deformation with ultrashort laser pulses," Appl. Phys. B **73**(4), 355-359 (2001).

70. A. V. Podlipensky, "Laser assisted modification of optical and structural properties of composite glass with silver nanoparticles" Ph.D. Thesis, Martin-Luther-Universität Halle-Wittenberg (2005).

71. A. Stalmashonak, G. Seifert, A. Abdolvand, *Ultra-short pulsed lased irradiation metal-glass nanocomposites*, Springer (2013).

72. User's manual of V-Lase & Green-Lase (B2.0)(2010) http://www.datalogic.com/eng/products/industrial-automation/laser-marking/vlase-pd-535.html (accessed February 2016).

73. S. G. Tomlin, "Optical reflection and transmission formula for thin films," J. Phys. D Appl. Phys. **1**(12), 1667–1671 (1968).

74. D. J. Sanders, "Temperature distributions produced by scanning Gaussian laser beams," Appl. Opt. **23**(1), 30 (1984).

75. A. L. Stepanov, D. E. Hole, and P. D. Townsend, "Modification of size distribution of ion implanted silver nanoparticles in sodium silicate glass using laser and thermal annealing," Nucl. Instrum. Meth. B **149**(1-2), 89–98 (1999).

76. G. Baffou and H. Rigneault, "Femtosecond-pulsed heating of gold nanoparticles," Phys. Rev. B **84**(3), 035415 (2011).

77. J. H. Yao, K. R. Elder, H. Guo, and M. Grant, "Theory and simulation of Ostwald ripening," Phys. Rev. B Condens. Matter **47**(21), 14110–14125 (1993).

78. G. Baffou, C. Girard, and R. Quidant, "Mapping heat origin in plasmonic structures," Phys. Rev. Lett. **104**(13), 136805 (2010).

79. C. Y. Tai and W. H. Yu, "The contribution of nonlocal electro-opto-thermal interaction to single molecule nonlinear Raman enhancement," Opt. Express **21**(21), 25026–25034 (2013).